

REPORT DOCUMENTATION PAGE				Form Approved OMB No. 0704-0188	
<p>The public reporting burden for this collection of information is estimated to average 1 hour per response, including the time for reviewing instructions, searching existing data sources, gathering and maintaining the data needed, and completing and reviewing the collection of information. Send comments regarding this burden estimate or any other aspect of this collection of information, including suggestions for reducing the burden, to the Department of Defense, Executive Service Directorate (0704-0188). Respondents should be aware that notwithstanding any other provision of law, no person shall be subject to any penalty for failing to comply with a collection of information if it does not display a currently valid OMB control number.</p> <p>PLEASE DO NOT RETURN YOUR FORM TO THE ABOVE ORGANIZATION.</p>					
1. REPORT DATE (DD-MM-YYYY) 10/01/2007		2. REPORT TYPE Final Technical Report		3. DATES COVERED (From - To) 10/01/2007 - 9/30/2008	
4. TITLE AND SUBTITLE Tracking Damage Nucleation and Propagation in Metallic Materials Using a Planar Biaxial Test System				5a. CONTRACT NUMBER	
				5b. GRANT NUMBER FA9550-07-1-0508	
				5c. PROGRAM ELEMENT NUMBER	
				5d. PROJECT NUMBER	
6. AUTHOR(S) Aditi Chattopadhyay				5e. TASK NUMBER	
				5f. WORK UNIT NUMBER	
7. PERFORMING ORGANIZATION NAME(S) AND ADDRESS(ES) Arizona State University Mechanical & Aerospace Eng P O Box 876106 Tempe, AZ 85287-6106				8. PERFORMING ORGANIZATION REPORT NUMBER N/A	
9. SPONSORING/MONITORING AGENCY NAME(S) AND ADDRESS(ES) Air Force Office of Scientific Research 875 N. Randolph Street Arlington, VA 22203				10. SPONSOR/MONITOR'S ACRONYM(S) AFOSR	
				11. SPONSOR/MONITOR'S REPORT NUMBER(S) AFRL-AFOSR-VA-TR-2016-630	
12. DISTRIBUTION/AVAILABILITY STATEMENT Unclassified Unlimited					
13. SUPPLEMENTARY NOTES					
14. ABSTRACT The major goals of the research project associated to the acquisition and installation of a biaxial/torsion testing system consist of two major tasks: (1) studying damage nucleation and accumulation of metallic materials and alloys under multiaxial conditions, including non proportional loading, and (2) detecting and characterizing damage under multiaxial loading using suitable NDE techniques, e.g., acoustic emission. This research will contribute and integrate well with the research tasks of the SHM MURI project currently being led by ASU.					
15. SUBJECT TERMS					
16. SECURITY CLASSIFICATION OF:			17. LIMITATION OF ABSTRACT	18. NUMBER OF PAGES	19a. NAME OF RESPONSIBLE PERSON Aditi Chattopadhyay
a. REPORT unclassified	b. ABSTRACT unclassified	c. THIS PAGE unclassified			19b. TELEPHONE NUMBER (include area code)

Tracking Damage Nucleation and Propagation in Metallic Materials Using a Planar Biaxial Test System

Technical Report

Reporting Period: 10/01/2007 to 9/30/2008

Program Manager: Victor Giurgiutiu

Sponsor Award No. FA9550-07-1-0508

Principal Investigator: Aditi Chattopadhyay

Co-PIs:

Pedro Peralta

Jun Wei

Arizona State University

1. Project Objectives

The major goals of the research project associated to the acquisition and installation of a biaxial/torsion testing system consist of two major tasks: (1) studying damage nucleation and accumulation of metallic materials and alloys under multiaxial conditions, including non-proportional loading, and (2) detecting and characterizing damage under multiaxial loading using suitable NDE techniques, e.g., acoustic emission. This research will contribute and integrate well with the research tasks of the SHM MURI project currently being led by ASU. It is expected that the project will be effective in: (i) characterizing the mechanical behavior of metallic and composite materials under 2-D stress states; (ii) tracking evolution and growth of damage such as fatigue cracks under multiaxial loading conditions; (iii) developing progressive damage laws under multiaxial cycle loading; (iv) developing *in situ* damage monitoring techniques for identification of crack nucleation and propagation in metallic materials.

2. Biaxial Tension/Torsion Test System

The MTS biaxial tension/torsion load frame is a custom designed testing system with 100 kN (22 kip) planar bi-axial load capacity and 1.1 kN-m (10 kip-in) torsion capacity along the horizontal (x) axis. The dimensions of the system are shown in Fig. 1. It was delivered by MTS to ASU on Sep. 12, 2008, approximately 1 year after placing the order, as required for appropriate design and manufacturing. Figure 2a shows the delivery of the system to ASU. On Oct. 1, 2008, MTS engineers came to ASU to setup, and calibrate the test frame, and to train ASU personnel on its operation and maintenance (Fig. 2b).

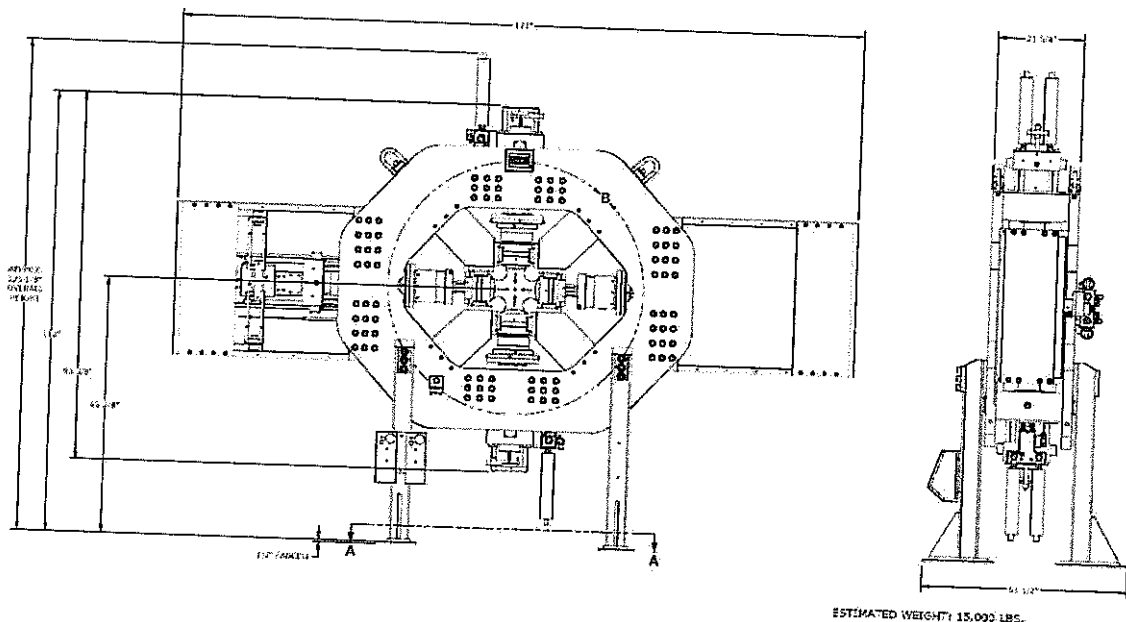


Fig. 1. Technical schematic of the MTS biaxial tension/torsion load frame.

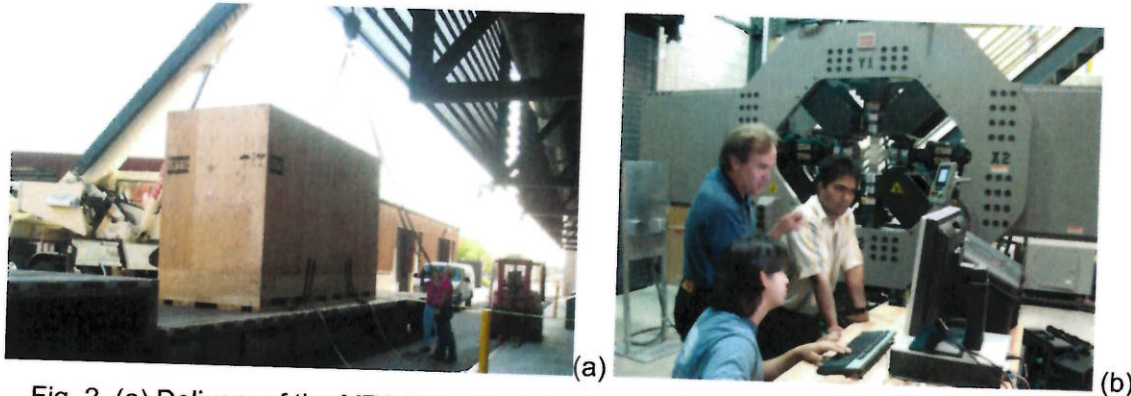


Fig. 2. (a) Delivery of the MTS biaxial tension/torsion load frame; (b) ASU graduate students being trained by an MTS engineer.

3. Approach and Accomplishments

3.1 Optimization of specimen geometry

The “standard” specimen chosen for testing in this frame is a modified cruciform sample. This cruciform specimen was optimized for in-plane tension-tension tests to achieve a uniform stress field in the gage area. Tubular specimens were fabricated for tension/torsion tests, but emphasis is being placed on the cruciform samples. The optimization process is described next

3.1.1 Metallic cruciform specimens

The two basic geometries considered initially for the cruciform samples are shown in Fig. 4.

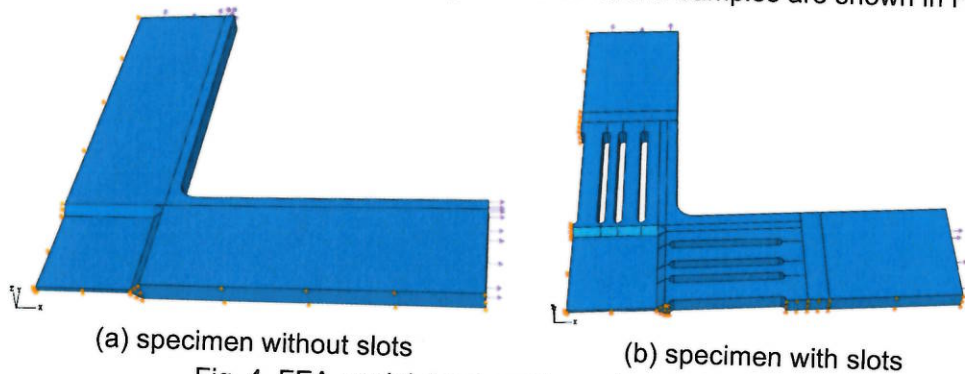


Fig. 4. FEA model, load and boundary conditions

These geometries, which were down-selected from several found in the literature, were studied using nonlinear finite element analysis (FEA), with emphasis on the radius of the corner fillet and the thickness of the gage section in the cruciform sample. Different corner fillets were simulated to avoid local stress concentrations. Various gage section geometries and slots in each arm were modeled to maintain a stress field as uniform as possible in the gage section. Due to the symmetry, only a quarter of the specimen is analyzed and symmetry boundary conditions are applied. The ratio of applied loads along the y (vertical) and x (horizontal) axes is

$P_y/P_x = 1.0$. Figure 5 shows contours of resultant displacement in the gage area of both the simple and slotted cruciform specimens obtained from FEA.

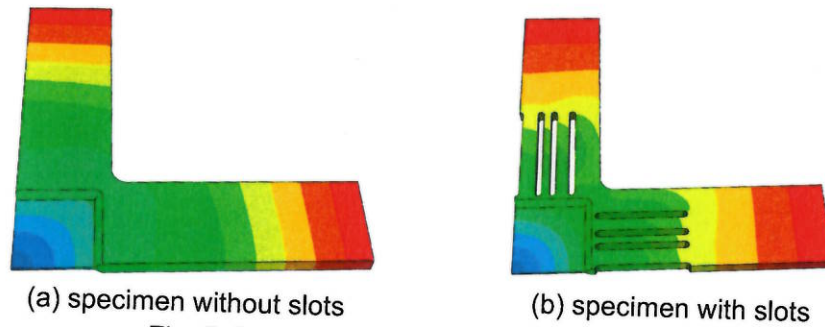


Fig. 5. Displacement distribution from FEA.

Figure 6 shows the Von Mises stress distribution for both geometries. It can be seen that the sample without slots shows higher stress concentrations at the corner between the gage area and the fillet while the stress distribution is uniform for the specimen with the slotted arms.

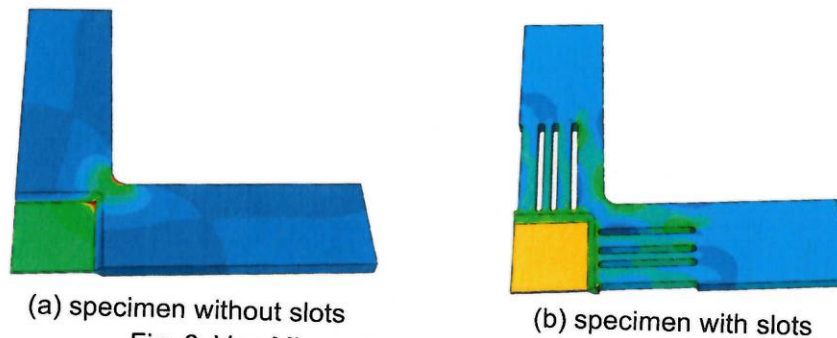


Fig. 6. Von Mises stress distribution from FEA.

Figures 7 and 8 show the maximum principal stress and in-plane shear stress distributions, respectively. The results indicate that the cruciform specimen with slots in the arms will generate an almost perfect two dimensional stress state within the gage area; therefore, that geometry was chosen for metallic samples.

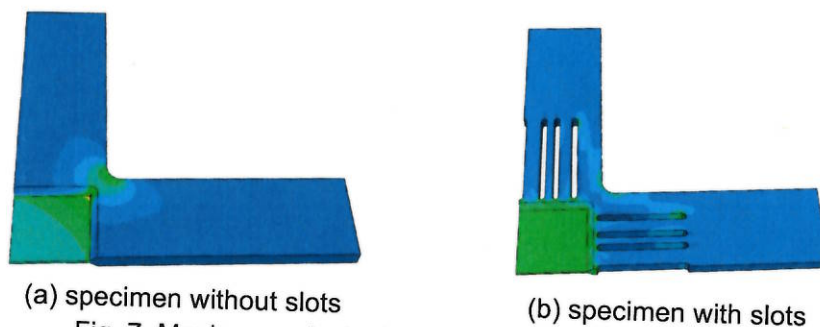


Fig. 7. Maximum principal stress distribution from FEA.

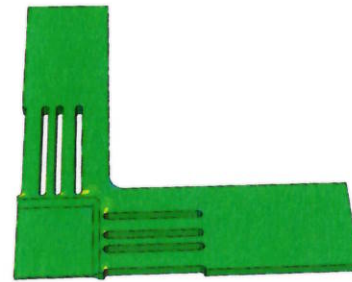
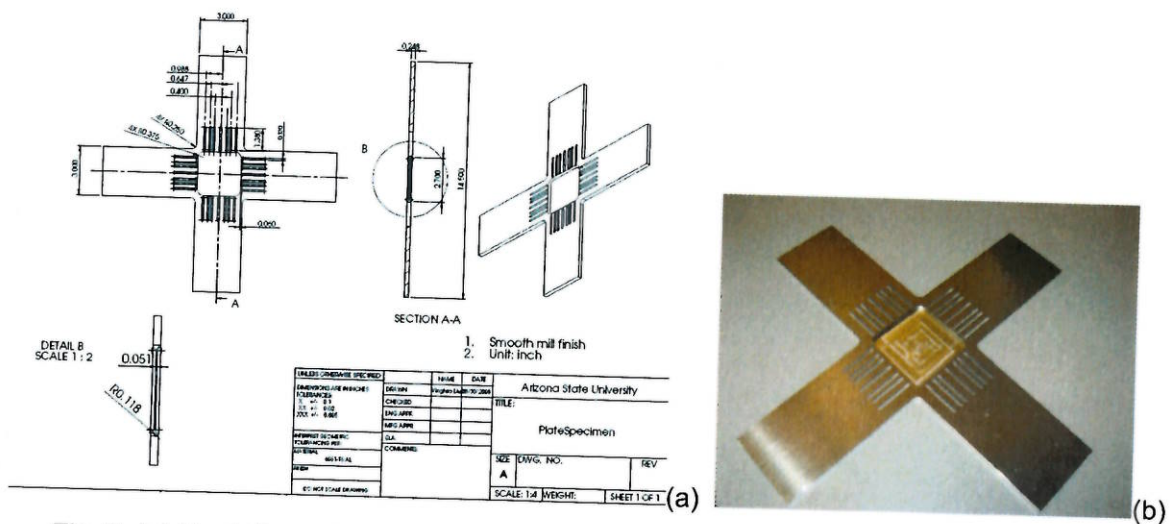
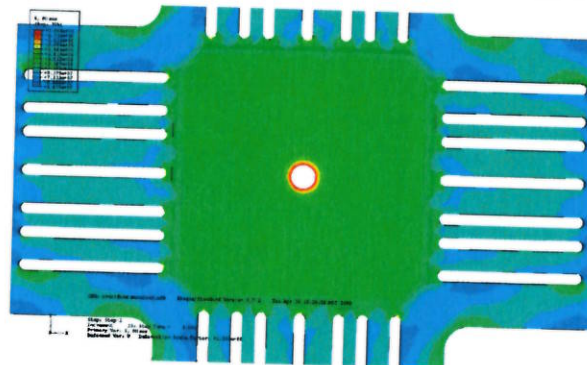


Fig. 8. In-plane shear stress distribution from FEA.

The final sample geometry and an example of a machined specimen are shown in Fig. 9.



A modified cruciform specimen with a central hole (Fig. 10) was also modeled under identical loads and used to study fatigue crack initiation at the inner circumference. The FEA shows a Mises stress concentration around the inner circumference that decreases away from the hole.



The basic geometry shown above was further modified to create a specimen that could be used to study correlations between microstructure and fatigue crack nucleation under biaxial loading. In particular, the sample had to be small enough to fit inside the scanning electron microscope, such that the microstructure around the central hole can be characterized and correlated to crack nucleation sites. This required scaling down the size of the sample significantly, i.e., sample length was reduced to 76.2 mm (3"). The sample fits inside the chamber of a Camscan Series 4 scanning electron microscope and will be attached to the grips of the biaxial frame using a system of collars. Figure 11 shows the geometry of the sample and the connectors as fabricated for testing, as well as results from FEA of the specimen to verify that the stress concentration around the central hole is indeed uniform despite the reduced sample size.

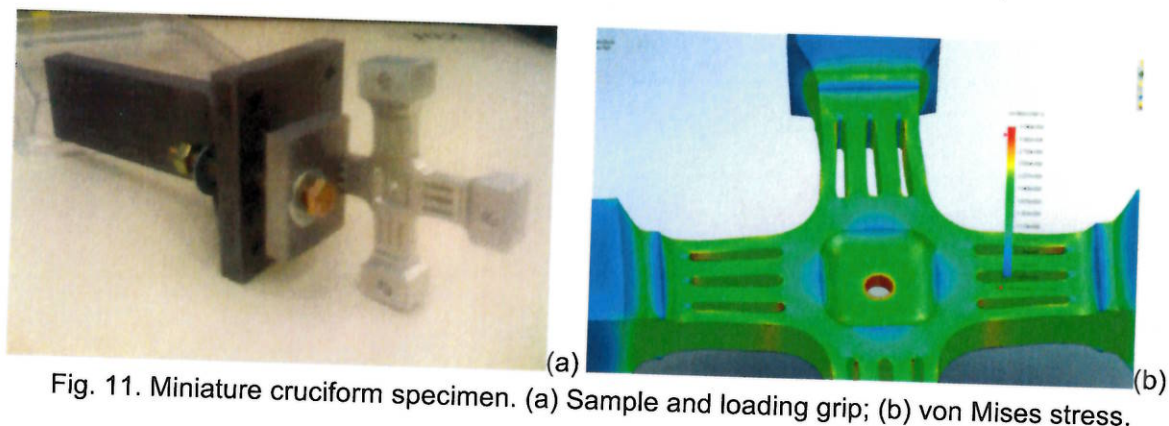


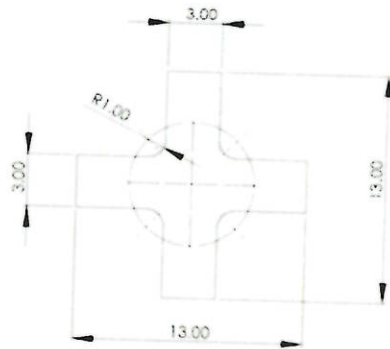
Fig. 11. Miniature cruciform specimen. (a) Sample and loading grip; (b) von Mises stress.

3.1.2 Cruciform specimens for composite materials

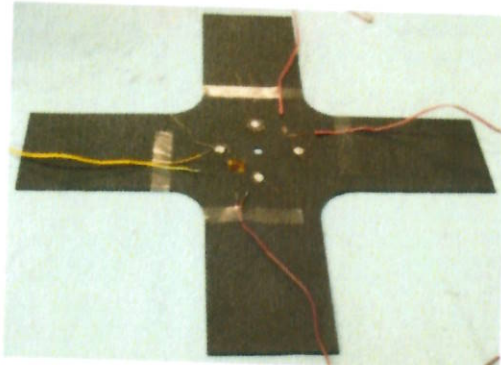
Composite structures are often subjected to complicated service loading conditions. These loading scenarios are very rarely uniaxial; therefore, two- or three-dimensional static and cyclic loading is necessary for realistic testing. In order to insure reliable operation and efficient design of these components, it is critical to characterize the material behavior under complex multiaxial loads. This information can then be used for structural health monitoring (SHM) and residual useful life estimation. In this regard, a series of tests were conducted using woven fiber composite specimens.

An optimal cruciform specimen also needed to be designed in this case. The design criteria included: (i) maximization of the gage region for uniform biaxial strains, (ii) minimization of the shear strains in the gage area, (iii) minimization of the stress concentrations outside of the gage section.

To investigate the effect of geometry on the stress concentration of the specimen, geometric parameters such as (i) the radius of the corner fillet at the intersection of the arms, (ii) the thickness of the gage area and (iii) the geometry of the gage area were considered. Some of the different geometries that were fabricated and tested are shown in Figures 12, 13 and 14. All of them included a central hole to induce crack nucleation at a controlled location.

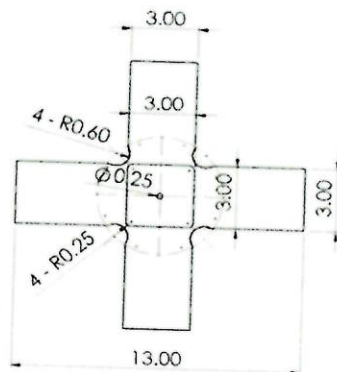


(a)

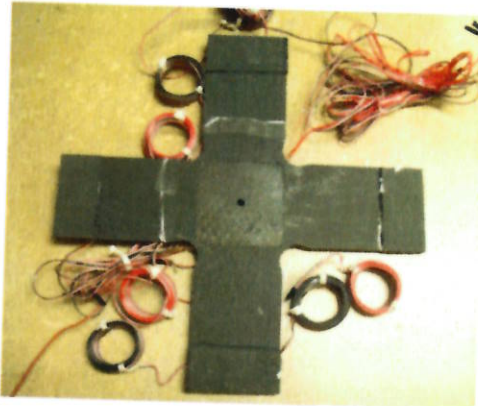


(b)

Fig. 12. Uniform thickness sample. (a) Geometry (in inches); (b) Fabricated specimen.

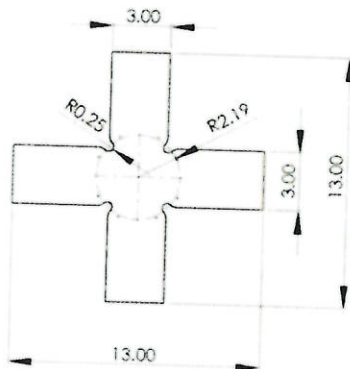


(a)



(b)

Fig. 13. Variable thickness sample. (a) Geometry (in inches); (b) Fabricated specimen.



(a)



(b)

Fig. 14. Variable thickness sample. (a) Geometry (in inches); (b) Fabricated specimen.

The gage area of the specimen shown in Fig. 12 is the same thickness as the arms and it has a 25.4 mm (1") radius of the fillet at the intersection of the arms, while the thickness of the gage area in Figures 13 and 14 is 1/3 of the thickness of the arms, and 15.24 mm (0.6") and 6.35 mm (0.25") radii for the corner fillets, respectively. Cracks should initiate at the central hole.

3.2 Tubular specimens

Tubular specimens were designed for tension/torsion as shown in Fig. 15. This loading has the advantage of providing variable principal directions for non-proportional loading. Figure 16 shows a specimen subjected to a tension/torsion cyclic loading. It can be seen that failure happened at the gage section, as expected.

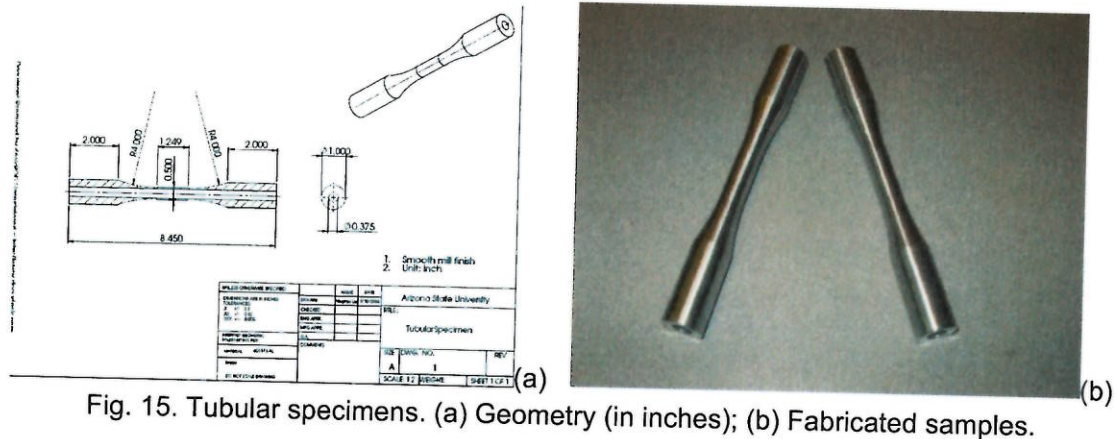


Fig. 15. Tubular specimens. (a) Geometry (in inches); (b) Fabricated samples.

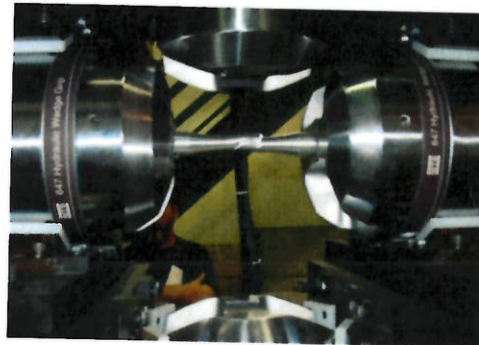


Fig. 16. Broken tubular specimen under tension/torsion cyclic loading

4. Applications of the Biaxial Frame

In this section, some applications of the biaxial frame will be reported for material and structural damage detection and residual useful life estimation.

4.1 Fatigue crack monitoring in metallic samples

The modified metallic cruciform specimen with central hole was tested under cyclic loading with a load ratio $R = 0.1$ and frequency of 10 Hz. The maximum applied load of 32 kN along both the x and y axes was based on the results of the nonlinear FE simulation, so that the von Mises stress around the hole was slightly lower than the yield strength of Al 2024, which was measured from a uniaxial test to be 325 MPa. The experimental test setup for the cruciform specimen, including the biaxial frame, the acoustic emission (AE) system, the data acquisition system (DAQ) and the CCD camera, is shown in Fig. 17.

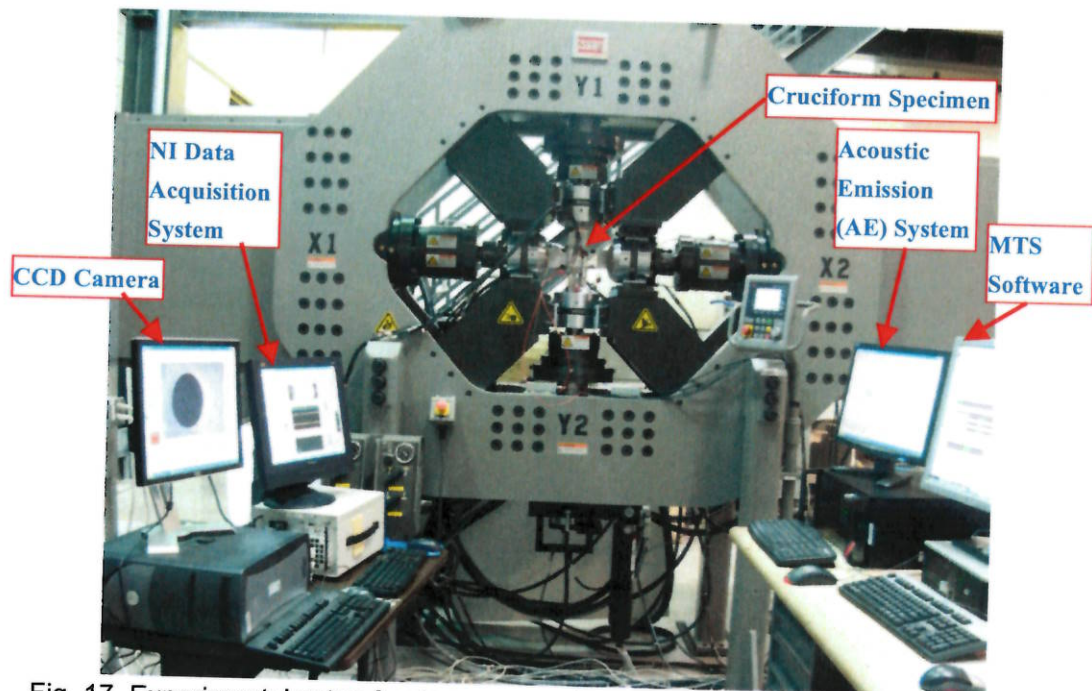


Fig. 17. Experimental setup for damage monitoring in a metallic cruciform specimen.

Figure 18 shows the placement of the AE and piezoelectric (PZT) transducers. In this setup, the AE sensors were used for crack monitoring and the PZT sensors for damage diagnosis and prognosis. Figure 19 shows the CCD camera used for monitoring crack propagation.

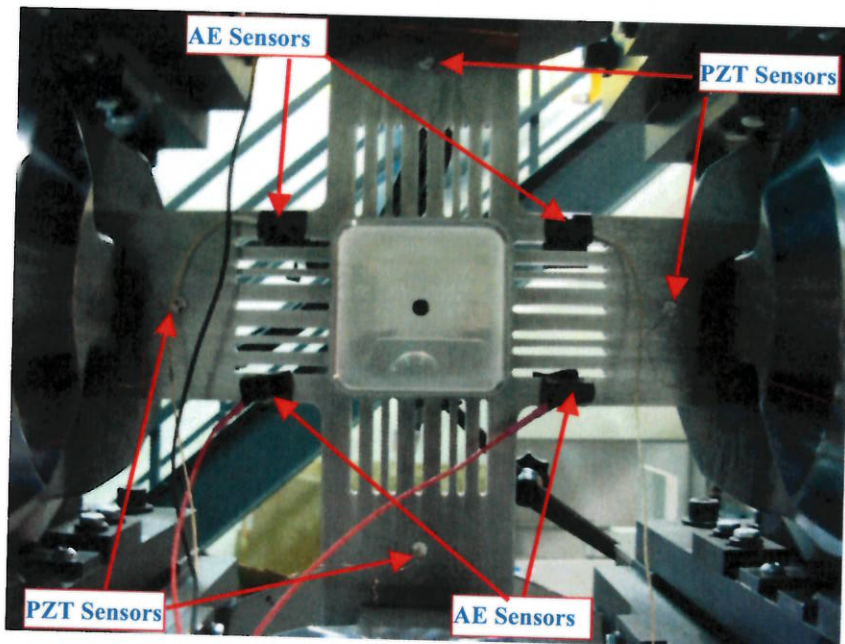


Fig. 18. Placement of AE and PZT sensors in a metallic cruciform sample.

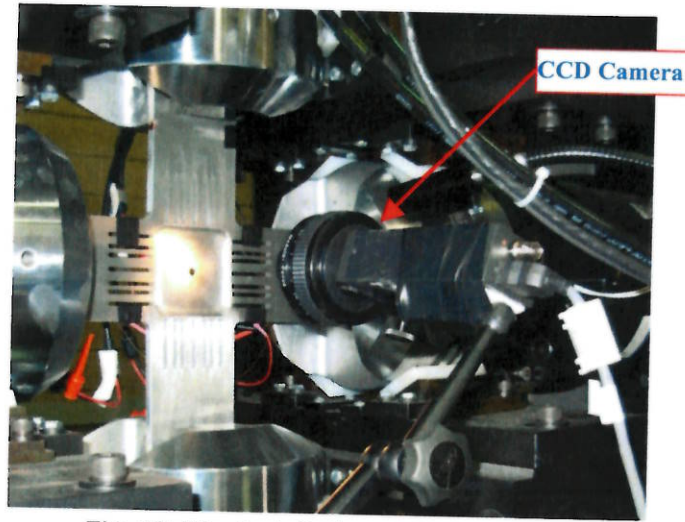


Fig. 19. The installation of CCD camera

Figure 20a shows a 1 mm long crack after 1598951 cycles. The AE amplitude then suddenly increased to 66 dB, as shown in Fig. 20 (b), which was probably due to rapid crack growth through the thickness of the specimen, as the initial crack probably had a thumbnail geometry.

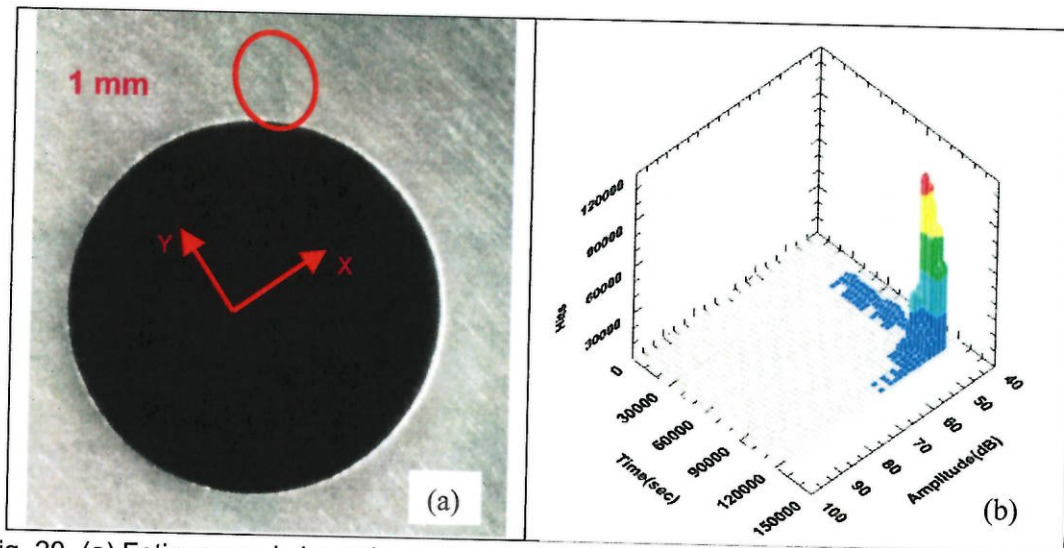


Fig. 20. (a) Fatigue crack 1 mm long observed at 1598951 cycles; (b) AE amplitude of 66 dB.

At 1610561 cycles, the crack reached a 4 mm length and the AE amplitude increased to 76 dB as shown in Fig. 21 (a) and (b). It should be noted that the crack initiation could occur at any place around the inner circumference of the hole and the crack could grow along either the x or the y direction based on the nonlinear FEA simulation shown in Fig. 11. The crack growth direction showed in Figures 20 and 21 is close the y direction, probably because it was parallel to the rolling direction of the 2024 Al plate used to fabricate the sample, and the rolling direction tends to be weaker with respect to crack propagation.

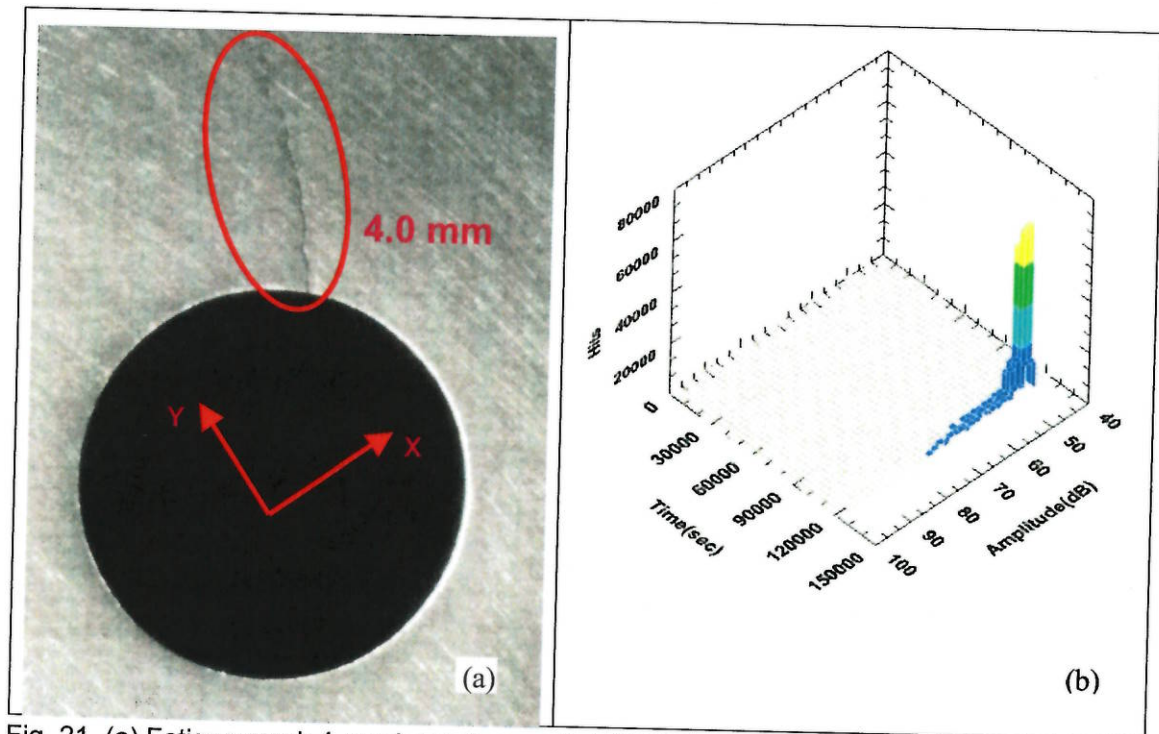


Fig. 21. (a) Fatigue crack 4 mm long observed at 1610561 cycles; (b) AE amplitude of 76 dB.

4.2 Structural health monitoring (SHM) on advanced composites

Although composite materials are being used in various structural systems such as aircrafts and automobiles, SHM and damage prognosis of composite materials are still emerging research areas. This section will report on the use of the biaxial frame for SHM of woven composites

4.2.1 Composite materials used in the test

Multiple carbon fiber polymer composite test coupons were fabricated in the AIMS center at Arizona State University. Woven fiber was purchased from Fiber Glast Inc. and the matrix used was HEXION EPON 863 and EPI-CURE 3290. A hot press was used to cure composite plates and the shapes of different coupons were cut using CNC machines. Different stacking sequences were also investigated to see how it affected the fatigue life of the coupon.

4.2.2 Uniaxial testing

Uniaxial tensile tests were completed to determine the tensile strength of the materials used in the biaxial test. An Eight-ply, quasi-isotropic woven composite sample was used in the test with a $[0^\circ/45^\circ/-45^\circ/90^\circ]_s$ stacking sequence. The monotonic tensile test followed the ASTM standard D 638. The geometry of the test coupon and examples of pristine and damaged samples are shown in Fig. 22. The measured strength of the composite coupons was used to estimate the cyclic load for the biaxial tension-tension fatigue test.

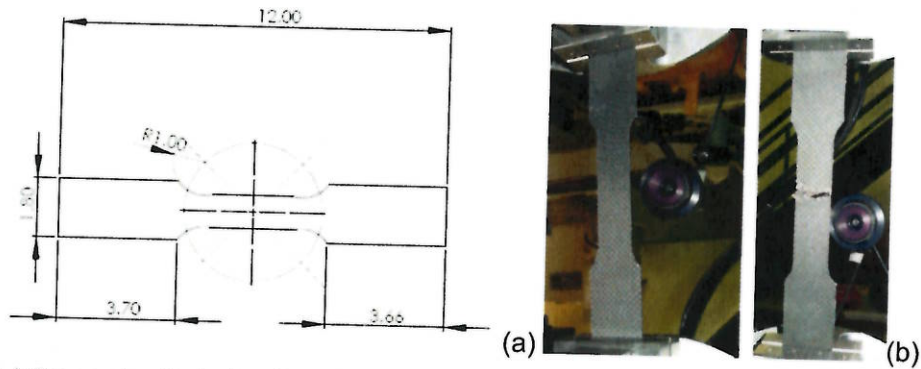


Fig. 22. (a) Geometry (in inches) of the composite dog bone sample. (b) Uniaxial loading test using composite dog bone samples.

4.2.3 Biaxial Test

The biaxial fatigue tests for composite cruciform specimens were conducted to study the performance of composite structures under complex loading conditions. In this work, multiple sensing techniques, such as AE, PZT active and passive sensing and strain gages were used to monitor the degradation process of the composite material. The experimental setup for the biaxial test is shown in Fig. 23.

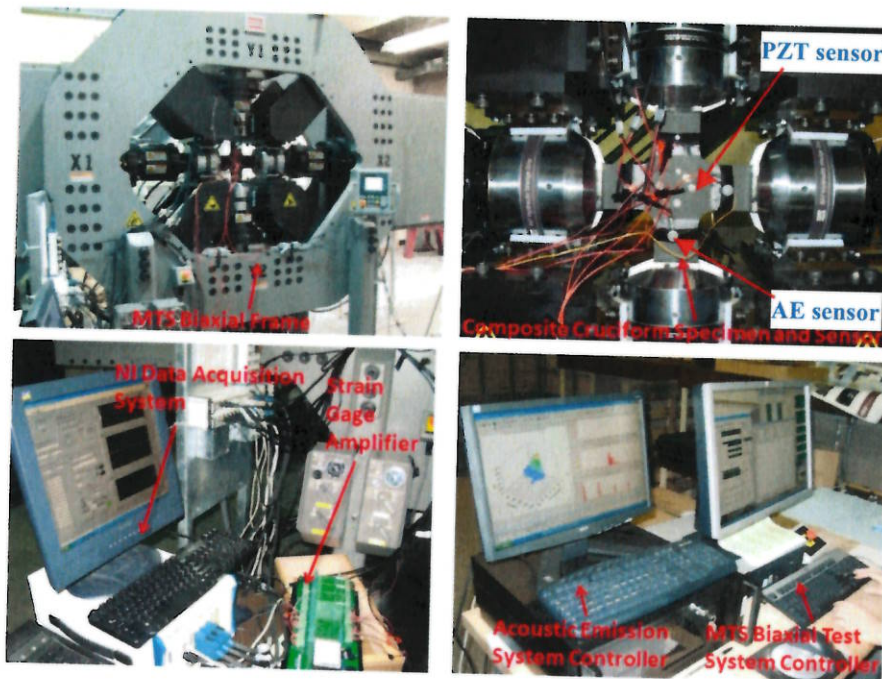


Fig. 23. Testing setup for composite cruciform samples under biaxial fatigue load.

The active PZT sensor signals were collected against three different types of actuation inputs: narrow band burst input, wide band chirp input and pseudo random pulse trains. The signal

features from various active and passive methods were being evaluated in the context of different metrics to eventually develop a high fidelity and robust prognostic algorithm. A time series prognostics algorithm based on a multivariate Gaussian process was used to map the input sensor signal features to a time varying damage index. In addition, the algorithm was used to forecast the future damage index and the corresponding residual useful life estimate (RULE). The prognostics framework will be verified by experiments with different biaxial loadings. The experimental excitation and sensing signals are shown in Figures 24 to 26.

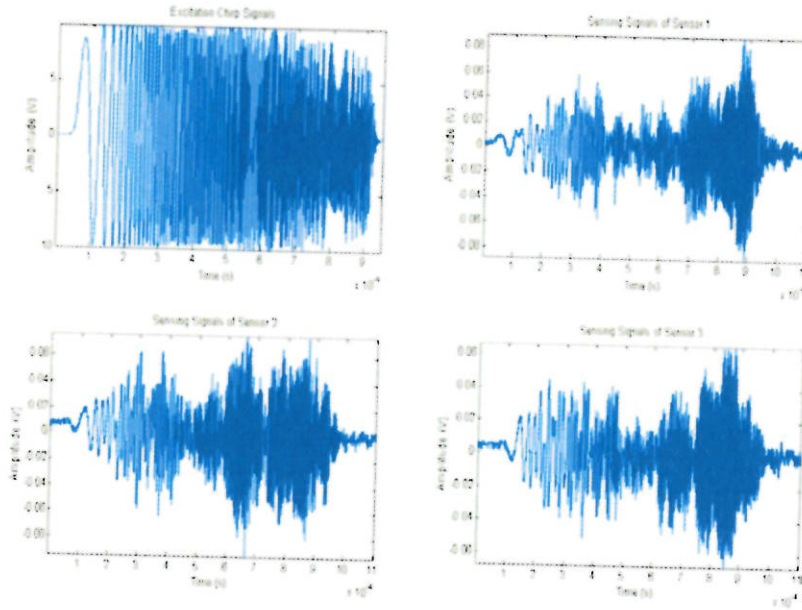


Fig. 24. Chirped excitation signals and related sensing signals.

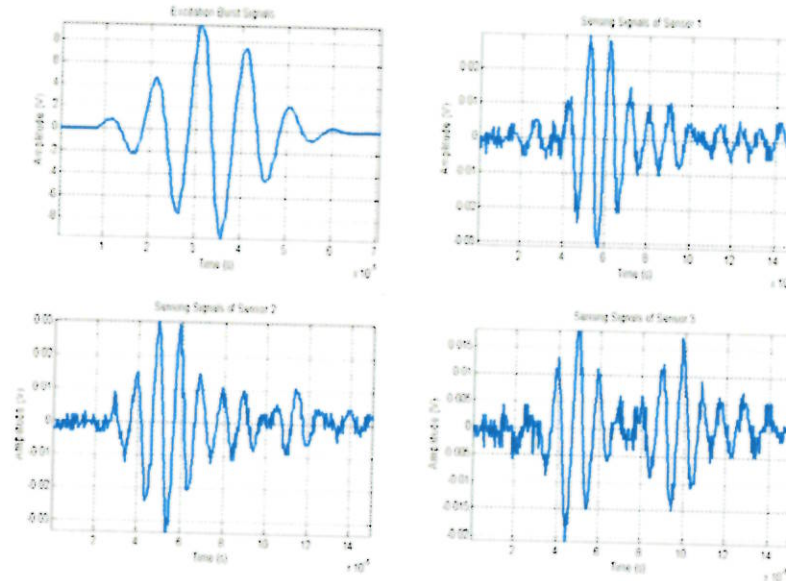


Fig. 25. Burst excitation signals and related sensing signals.

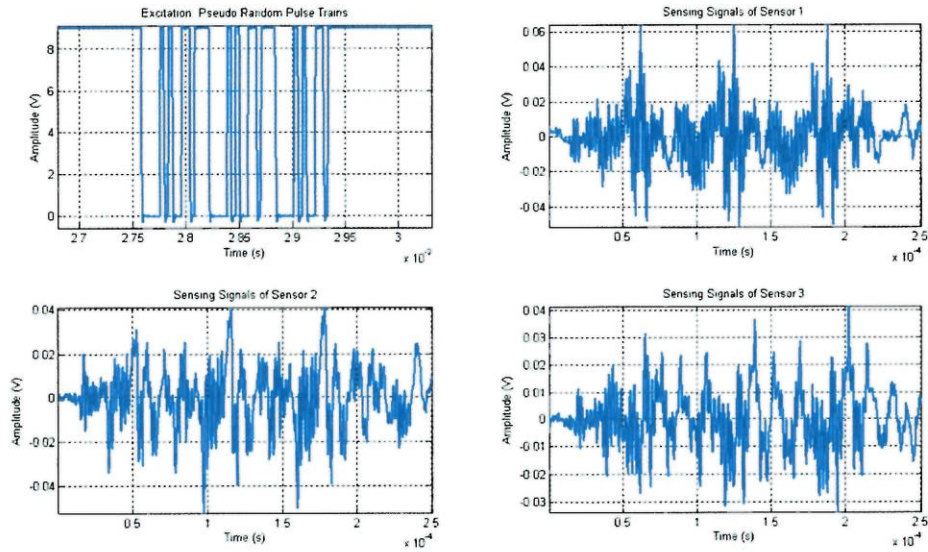


Fig. 26. Pseudo random pulse trains and related sensing signals

Acoustic emission techniques were also used during this test. Four sensors were mounted on the coupon and the counts associated to acoustic events indicated a clear trend in the degradation process. The AE counts are a good choice at later stages of fatigue life because a large amount of high-energy acoustic bursts were released as damage occurred. In Fig. 27, the number of counts, amplitude and time are shown. Note the steady increase of the amplitude up to 92 dB indicating the growth of damage.

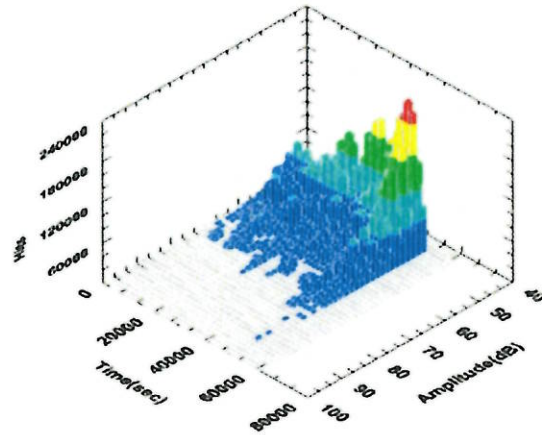


Fig. 27. Acoustic emission Hits vs. Time (sec) and Amplitude (dB) during testing.

4.3 SHM on a metallic specimen

In this application, a correlation analysis approach based on non-parametric system identification is used to estimate the current damage state. This damage state is estimated by correlating the real-time sensor signals obtained from two different strain gages placed at two

different places on the structure/specimen. Once the damage state (in the form of a damage index) is estimated, it is fed to an off-line predictive model based on a Gaussian process to forecast the future damage state and the residual useful life. The real-time algorithm was validated on an Al-6061 cruciform specimen undergoing biaxial fatigue loading. The details on the application of this procedure are provided in the paper included in the appendix.

5. Outreach

5.1 Local schools

The Kyrene Middle School Prep. Program (8th grade), AZ, visited the Biaxial Testing Facility on 4/30/09. These students were given a laboratory tour and some basic instruction (visual) on multi-axial loading using the biaxial test frame. A picture is shown in Fig. 28.



Fig. 28. Kyrene Middle School, AZ, students visit the biaxial testing facility.

5.2 AFOSR sponsored research

The program managers of the SHM MURI project, Dr. Victor Giurgiutiu and Dr. David Stargel from AFOSR, and members of the MURI Advisory Board visited the Biaxial Testing facility on 5/19/09. They were given a demonstration of the use of the frame on SHM of metallic materials and were shown the corresponding testing setups, as shown in Fig. 29.



Fig. 29. MURI program managers and advisory board members visit the biaxial testing facility.

6. Publications

- S. Mohanty, A. Chattopadhyay, J. Wei, and P. Peralta, On-line Structural Health Monitoring and Prognosis of a Biaxial Cruciform Specimen, 50th AIAA/ASME/ASCE/AHS/ASC Structures, *Proc. Structural Dynamics and Materials Conference*, Palm Springs, California, 4–7 May 2009.
- S. Lemmer, C. Leser, P. Peralta, and A. Chattopadhyay, "Apparatus for Biaxial Thermal Fatigue Testing." *Proceedings of the 7th International Conference on Fatigue Damage of Structural Materials*, Sept. 2008.

7. Summary

- Optimized cruciform specimens for metallic materials
- Optimized cruciform specimens for advanced composite materials
- Designed and fabricated miniature cruciform samples to study crack nucleation
- Designed tubular metallic specimen for tension/torsion testing
- Conducted crack initiation test via AI 2024 cruciform specimens
- Conducted SHM validation test via AI 2024 cruciform specimens
- Conducted SHM validation test via woven composites cruciform specimens

8. Appendix

On-line Structural Health Monitoring and Prognosis of a Biaxial Cruciform Specimen

Subhasish Mohanty * Aditi Chattopadhyay † Jun Wei ‡

Pedro Peralta§

Mechanical and Aerospace Engineering, Arizona State University, Tempe, AZ, 85287, USA

The current research of on-line damage state estimation techniques offers adaptive damage state prediction and residual useful life assessment. The real-time damage state information from an on-line state estimation model can be regularly fed to a predictive model to update the residual useful life estimation in the event of a changing situation. The present paper discusses the use of an integrated prognosis model, which combines an on-line state estimation model with an off-line predictive model to adaptively estimate the residual useful life of an Al-6061 cruciform specimen under biaxial loading. The overall fatigue loading history is assumed to be a slow time scale process compared to the time scale at which, the sensor signals are acquired for on-line state estimation. The fast scale on-line model is based on a non-parametric system identification approach such as correlation analysis. A new damage index equivalent to quantitative damage state information at any particular fatigue cycle, is proposed. The on-line model regularly estimates the current damage state of the structure based on passive strain gauge signals. These damage states information is regularly fed to the slow scale off-line predictive model as it becomes available. The off-line predictive model is a probabilistic nonlinear regression model, which is based on Bayesian statistics based Gaussian process approach. The off-line module adaptively updates the model parameters and recursively predicts the future states to provide residual useful life estimate.

Nomenclature

Fast scale variables

m	Fast scale lag numbers
Δt	($= 1/f_f$) Fast scale time interval
T	Fast scale observation time
M	No. of fast scale observation samples
$u(m)$	Fast scale input observation at lag m
$v(m)$	Fast scale output observation at lag m
$\nu(m)$	Fast scale noise observation at lag m
$\gamma_{uv}(m)$	Fast scale cross correlation coefficient at lag m

Slow scale variables

n	Slow scale damage level number (or damage instances) (Note: In general n is not same as number of fatigue cycles)
\bar{n}	Number of damage instances after last fast scale data available
\bar{n}^*	After last fast scale data available, the number of damage instances to damage state become critical
N	Total no. of fatigue cycles
N_0	No. of fatigue cycles elapsed, before the first on-line sensor data available

*Graduate Research Associate, Mechanical and Aerospace Engineering, Arizona State University, Tempe, AZ, 85287, USA, and AIAA Student member.

†Professor, Mechanical and Aerospace Engineering, Arizona State University, Tempe, AZ, 85287, USA, and Fellow AIAA.

‡Research faculty, Mechanical and Aerospace Engineering, Arizona State University, Tempe, AZ, 85287, USA

§Associate Professor, Mechanical and Aerospace Engineering, Arizona State University, Tempe, AZ, 85287, USA

ΔN	No. of fatigue cycles per increment of each damage instant
θ_n^d	Slow scale material scatter related noise hyperparameter at n^{th} fatigue cycles
θ_n^p	Slow scale process hyperparameter at n^{th} damage instances
θ_n^w	Slow scale input weighing hyperparameter at n^{th} damage instances
θ_n^b	Slow scale input bias hyperparameter at n^{th} damage instances
\mathbf{x}_n	Slow scale input vector at n^{th} damage instances with $n = 1, 2 \dots, n, \dots, N$
\bar{a}_n	Slow scale output damage index at n^{th} fatigue cycles with $n = 1, 2 \dots, n, \dots, N$
\mathbf{K}_n	Slow scale kernel matrix at n^{th} fatigue cycles with $n = 1, 2 \dots, n, \dots, N$
$k(\mathbf{x}_i, \mathbf{x}_j)$	Slow scale kernel function at n^{th} fatigue cycles with $i, j = 1, 2 \dots, n, \dots, N$

I. Introduction

Real-time health monitoring and prognostics is emerging at the forefront of Condition based Maintenance (CBM) of critical structural systems giving rise to the term Prognostic Health Management (PHM). Whether it is a newly acquired or an aging fleet aircraft, the structural life ceiling of the fleet aircraft are defined from three distinct approaches: safe-life, fail-safe, and damage-tolerant approaches. A detailed review of these approach and their applications to US Navy's P-3C aircraft is presented by Iyer, et. al.¹ In the case of safe-life approach service or retirement life of a component is defined by crack initiation time derived from a full-scale component, or element fatigue test. In practice, however, the component is retired before the formation of a fatigue crack by using safety factors on calculated crack initiation time because of inherent variability in both static and fatigue material properties as well as assumptions made in analytical models used to calculate crack initiation time. The fail-safe approach assumes an initial damage due to manufacturing and its subsequent growth during service to detectable crack sizes. Service life in fail-safe structures can thus be defined as the time to a survivable detectable damage. The fail-safe approach requires inspections as part of the maintenance program, and these inspections are also specifically geared to find damages in identified critical components of the aircraft. In the case of damage-tolerant approach, it assumes initial defects, however small they may be in critical structural elements, which will eventually grow in service to large crack sizes. Service life is estimated through rigorous crack growth analysis both deterministic and stochastic. A majority of the deterministic crack growth analysis models are based on the approach followed in FASTRAN² or AFGROW³ type crack growth model. It is to be noted that these models are based on some empirical parameters, which have to be tuned for a particular application. In case of stochastic life estimation, two different approaches, are currently being used in industry, and are these techniques are continuously being improved by the stochastic life modeling research community. In the first technique service life is based on the basic principles of Miner's damage accumulation criteria, and in the second technique the stochastic crack growth curves are obtained first, followed by estimation of the corresponding stochastic service life. Wu and Ni⁴ presented a stochastic crack growth model which can be used for stochastic life estimation of structures. In the case of damage accumulation type models, the recent work by Liu and Mahadeven⁵ on nonlinear fatigue damage accumulation rule and a stochastic S-N curve representation technique for predicting stochastic fatigue life under variable amplitude loading is noteworthy. In the above mentioned deterministic or stochastic approaches the damage tolerance and fatigue life predictions are obtained based on assumed structural flaws or based on previous coupon test results regardless of whether the assumed structural flaws actually occur in service (i.e., prognosis is made before diagnosis). In addition in a real life scenario, changing loading conditions and other environmental conditions such as change in humidity and temperature, leads to different crack growth law parameters, compared to those originally found from coupon testing. Consequently, a large degree of conservatism is incorporated into structural designs due to these uncertainties. The current research in the area of on-line⁶⁻⁸ damage state estimation, or Structural Health Monitoring (SHM) techniques offers methodologies for adaptive damage state prediction and residual useful life assessment. The on-line state estimation model can be either supervised or baseline-free unsupervised model. In a supervised approach,^{7,8} the model has to be trained for known damage cases based on previously conducted tests. The supervised model is difficult to implement in real-life condition. This is because of the changing boundary conditions and noise levels (due to electrical connections), which may not necessarily be similar to the previously obtained data (those used for training purpose). A detail review on different SHM approaches are presented by Farrar, et. al.^{9,10} For real-time damage monitoring and prognosis, there is also a need for an effective predictive model to forecasts the future state and the remaining life of the

structure. The real-time damage state information from the on-line state estimation model can be regularly fed to the predictive model to update the residual useful life estimation in the event of a changing situation. The bearing failure adaptive predictive model presented by Billington, et.al.¹² is among the few earliest reported work on real-time adaptive predictive models. However, the model is based on a linear covariance structure, which may not always be suitable for learning nonlinear damage growth dynamics. The present paper proposes a recursive Gaussian process predictive model, in which the model parameters are adaptively updated to predict the future states and residual useful life estimate. Unlike the covariance based structure, the Gaussian process¹³⁻¹⁵ uses the kernel function. The kernel function is a multi-dimensional function and transfer the linearly inseparable information first to a high dimensional feature space, where the information can be linearly separable. In the present paper a non-parametric system identification based correlation analysis approach is used to estimate the current damage state. The current damage state is estimated by correlating the real-time sensor signals obtained from two different strain gauges placed at two different places on the structure. Once the damage state (in the form of a damage index) is estimated, it is fed to the Gaussian process off-line predictive model to forecast the future damage state and residual useful life estimate (RULE). The real-time algorithm is validated on a Al-6061 cruciform specimen undergoing biaxial fatigue loading.

II. Integrated Prognosis Model

The integrated prognosis model is a real-time prognosis model, that work in conjunction with real-time sensor signal measurements. As shown in Fig. 1, the integrated prognosis architecture has two distinct sub modules, the on-line state estimator and the off-line state predictor. The on-line state estimator infers the current state of the structure from real-time sensor measurements. Once the current on-line state information becomes available, it is fed to the off-line predictive model to predict the future states and compute the corresponding residual useful life estimate. It is noted that the overall fatigue loading history is assumed to be a slow time scale process⁶ compared to the time scale at which the sensor signals are acquired at discrete intervals. Based on this assumption, from this point onwards the sensor signal acquiring process and corresponding current cycle damage state (or damage index) estimation process is denoted a fast scale process, whereas the overall slower fatigue process is denoted a slow scale process. It is noted that the fast scale sensor measurements are performed at discrete slow scale intervals. Also, it is noted that at the individual slow scale instances, where the fast scale sensor measurements are taken, the damage state of the structure is assumed to remain unchanged.

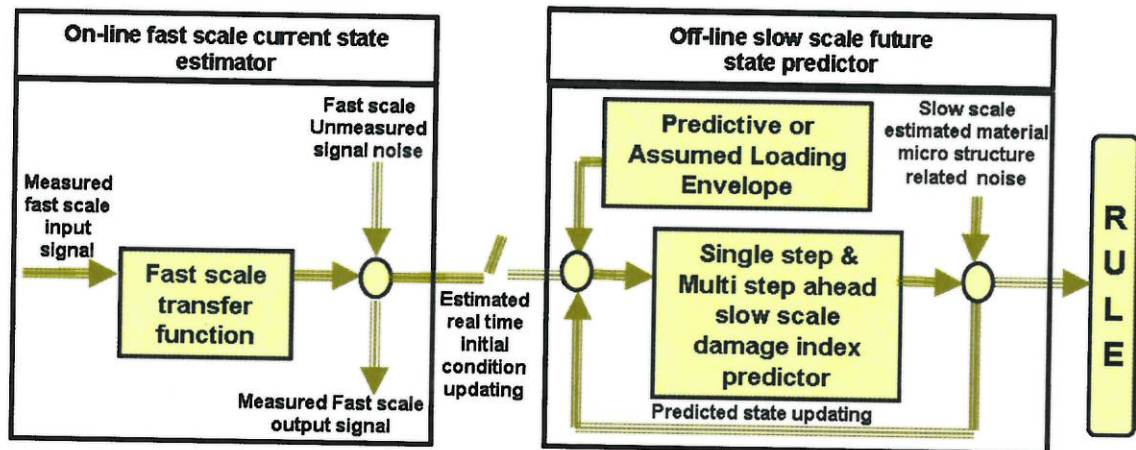


Figure 1. Schematic of integrated prognosis model.

A. On-line fast-scale damage state estimation

1. Fast-scale transfer function

At any given n^{th} slow scale fatigue cycle the fast scale output sensor measurement can be mapped with the fast scale input sensor measurement over fast scale unmeasured noise ν . A typical n^{th} fatigue cycle block diagram that maps the fast scale input measurement with fast scale output measurement is shown in Fig. 2. The fast scale Z-domain transfer function $P(z)$ between input u and output y at n^{th} damage level can be represented as:

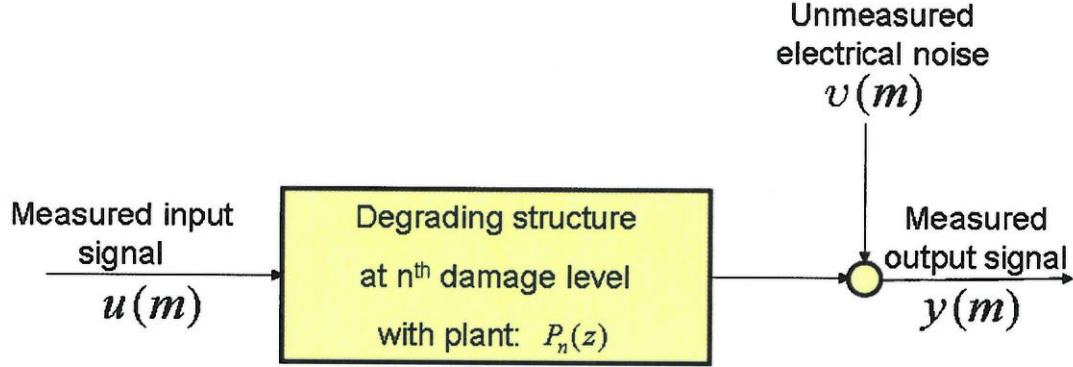


Figure 2. Block diagram for fast scale transfer function. The transfer function is an instantaneous representation of the time degrading structure at any typical damage level. However as the damage grow the transfer function also changes leading to a time variant approach for system identification.

$$\begin{aligned} v(t) &= P(z)u(t) + \nu(t) \\ &= (b_0 + b_1z^{-1} + b_2z^{-2} + \dots + b_Mz^{-M})u(t) + \nu(t) \end{aligned} \quad (1)$$

where $z^{-m}; m = 0, 1, \dots, M$ are the backspace operators of the pulse transfer function $P(z)$ and $b_m; m = 0, 1, \dots, M$ are the finite impulse response (FIR) coefficients. Then Eq. (2) can be rewritten in the discrete domain as

$$v(t) = b_0u(t) + b_1u(t-1) + b_2u(t-2) + \dots + b_Mu(t-M) + \nu(t) \quad (2)$$

2. Damage index

The slow scale damage index $a(n)$, at n^{th} fatigue cycle, is the representative damage state inferred from n^{th} fatigue cycle fast scale sensor measurements. The damage index can be derived by finding the m^{th} lagged output $v(t+m)$ from Eq. (2) and pre multiplying the input $u(t)$, obtaining

$$u(t)v(t+m) = b_0u(t)u(t+m) + b_1u(t)u(t-1+m) + b_2u(t)u(t-2+m) + \dots + b_Mu(t)u(t-M+m) + u(t)\nu(t+m) \quad (3)$$

Applying expectation operator to both sides of Eq. (3) and assuming independence between noise and the input signal, the m^{th} lagged cross-correlation coefficients can be expressed as

$$\gamma_{uv}(m) = b_0\gamma_{uv}(m) + b_1\gamma_{uv}(m-1) + b_2\gamma_{uv}(m-2) + \dots + b_M\gamma_{uv}(m-M) \quad ; m = 0, 1, \dots, M \quad (4)$$

With known input (u) and output (v) time series, the m^{th} lagged cross-correlation coefficients $\gamma_{uv}(m)$ and auto-correlation coefficients $\gamma_u(m)$, the FIR coefficients $b_m; m = 0, 1, \dots, M$ can be estimated and hence the n^{th} fatigue cycle pulse transfer function. To estimate $M+1$ FIR coefficients we need to solve $M+1$ algebraic equations given by Eq. (4). However, solving $M+1$ algebraic equations involves inverting a $(M+1) \times (M+1)$ autocorrelation coefficient matrix, which becomes computationally expensive in the context of real-time applications. To circumvent this problem rather than directly estimating the transfer function and the damage states (such as n^{th} fatigue cycle zeros and poles), the damage state equivalent

damage index can be estimated. Based on the cross-correlation coefficients $\gamma_{uv}(m)$ a new damage index is formulated, which is expressed as follows:

$$a_n = \sqrt{\frac{\sum_{m=0}^{M-1} (\gamma_{uv}^n(m) - \gamma_{uv}^0(m))^2}{\sum_{m=0}^{M-1} (\gamma_{uv}^0(m))^2}}; n = 1, 2, \dots, N/\Delta N \quad (5)$$

where $\gamma_{uv}^n(m)$ represents n^{th} fatigue cycle fast scale cross-correlation coefficients, and $\gamma_{uv}^0(m)$ represents 0^{th} (or reference) fatigue cycle fast scale cross-correlation coefficients. It is noted that if $\max\{\gamma_u(m) \text{ or } \gamma_v(m)\} = 1$; $m = 0, 1, \dots, M$, then either the sensor is damaged or is debonded, producing only noise.

B. Off-line slow-scale damage state prediction and residual useful life estimation

1. Predicting in a Bayesian framework

The goal of a probabilistic Bayesian¹³⁻¹⁵ forecasting approach is to compute the posterior distribution¹¹ of a future damage state or damage index a_{n+1} , i.e., to determine the probability distribution of the random damage index a_{n+1} given a random test input \mathbf{x}_{n+1} and a set of n training data points described as $D = \{\mathbf{x}_i, a_i\}_{i=1, \dots, n}$. In the Bayesian framework the predictive distribution with mean and variance can be found by conditioning the damage indices $a_1, a_2, \dots, a_n, a_{n+1}$ that are affected by the corresponding random inputs $\mathbf{x}_1, \mathbf{x}_2, \dots, \mathbf{x}_n, \mathbf{x}_{n+1}$. A prior over the space of possible functions to model the random damage index as $f(a|\alpha)$, can be defined where α are some hyperparameters that can account for random load sequence effect in the form of curve fitting. Also, a prior over the noise $f(\vartheta|\beta)$, can be defined where ϑ is some appropriate noise vector that arises due to scatter in material micro structure and β is another set of hyperparameters used to model the uncertainty due to scatter. Now if the hyperparameters α and β are given, the conditional probability¹³⁻¹⁵ can be expressed as

$$f(a_{n+1} | \{\mathbf{x}_{i=1, \dots, n}, \alpha, \beta\}) = \int f(a_{n+1} | \{\mathbf{x}_{i=1, \dots, n}, a, \vartheta\}) f(a|\alpha) f(\vartheta|\beta) da d\vartheta \quad (6)$$

where a and ϑ denotes the underlying function which respectively corresponds to damage index and noise due to scatter. Since a_1, a_2, \dots, a_n , and a_{n+1} are conditioned random variables in the observed set of damage indices, the conditional distribution of a_{n+1} can be written as follows

$$f(a_{n+1} | D = \{\mathbf{x}_i, a_i\}_{i=1, \dots, n}, \mathbf{x}_{n+1}, \alpha, \beta) = \frac{f(a_{n+1} | \{\mathbf{x}_i\}_{i=1, \dots, n+1}, \alpha, \beta)}{f(a_n | \{\mathbf{x}_i\}_{i=1, \dots, n}, \alpha, \beta)} \quad (7)$$

2. Predicting with a Gaussian process

To evaluate Eq. (7) it is necessary to evaluate the integral given in Eq. (6). However, in general, Eq. (6) is complicated to evaluate. The standard approach to evaluate the integral in Eq. (6) is by a method called evidence maximization¹⁶ or by numerically integrating by Monte Carlo simulation.¹⁷ However, assuming the underlying damage index function $a_{i=1, \dots, n, n+1, \dots}$ follows a Gaussian distribution, the exact analytical form of Eq. (7) is as follow

$$f(a_{n+1} | \{x_i\}_{i=1, \dots, n}, \mathbf{K}_{n+1}) = \frac{1}{(2\pi)^{n+1/2} \det(\mathbf{K}_{n+1})^{1/2}} \exp\left(-\frac{1}{2}(\mathbf{a}_{n+1} - \mu)^T \mathbf{K}_{n+1}^{-1} (\mathbf{a}_{n+1} - \mu)\right) \quad (8)$$

where μ is the function mean and \mathbf{K}_n is a $n \times n$ kernel matrix. The individual elements k_{nmn} of the kernel matrix \mathbf{K}_n can be found from a parameterized kernel function that will be described in the next section. Assuming zero mean function distribution Eq. (8) can be written as

$$\begin{aligned} f(a_{n+1} | D = \{\mathbf{x}_i, a_i\}_{i=1, \dots, n}, \mathbf{x}_{n+1}, k_{ij}(x_i, x_j, \Theta)_{i,j=1,2, \dots, n+1}) \\ = \sqrt{\frac{\det(\mathbf{K}_n)}{(2\pi)\det(\mathbf{K}_{n+1})}} \exp\left(-\frac{(a_{n+1} - \hat{a}_{n+1})^2}{2\sigma_{\hat{a}_{n+1}}^2}\right) \end{aligned} \quad (9)$$

where \hat{a}_{n+1} is the one-step ahead predicted mean at slow scale damage level $n + 1$ and is given by

$$\hat{a}_{n+1} = \mathbf{k}^T \mathbf{K}_n^{-1} \mathbf{a}_n; \quad k_i = k(\mathbf{x}_{n+1}, \mathbf{x}_i)_{i=1,2,\dots,n} \quad (10)$$

whereas $\sigma_{\hat{a}_{n+1}}^2$ is the one-step ahead predicted variance at slow scale damage level $n + 1$ and is given by

$$\sigma_{\hat{a}_{n+1}}^2 = \kappa - \mathbf{k}^T \mathbf{K}_n^{-1} \mathbf{k}; \quad k_i = k(\mathbf{x}_{n+1}, \mathbf{x}_i)_{i=1,2,\dots,n}; \quad \kappa = k(\mathbf{x}_{n+1}, \mathbf{x}_{n+1}) \quad (11)$$

3. Parameterizing the kernel function

There are many possible choices of prior interpolating kernel functions. From a modeling point of view, the objective is to specify a prior kernel function that contains our assumptions about the structure of the process being modeled. Formally, it is required to specify a function that will generate a positive definite kernel matrix for any set of inputs. In this paper, a multi layer perceptron (MLP)¹⁸ based kernel function is used, which has the following form

$$k_f(\mathbf{x}_i, \mathbf{x}_j, \Theta) = \theta_n^p \text{Sin}^{-1} \frac{\mathbf{x}_i^T \theta_n^w \mathbf{x}_j + \theta_n^b}{\sqrt{(\mathbf{x}_i^T \theta_n^w \mathbf{x}_i + \theta_n^b + 1)(\mathbf{x}_j^T \theta_n^w \mathbf{x}_j + \theta_n^b + 1)}} + \theta_n^v \quad (12)$$

In Eq. (12) the superscript n represents the n^{th} damage instances. It is noted that unlike the fixed hyperparameters, the hyperparameters in Eq. (12) are adaptively found as new data set $D = \{\mathbf{x}_i, a_i\}_{i=1,\dots,n,n+1,\dots,N}$ becomes available.

4. Hyperparameters determination

So far we have only considered the properties of the prediction model for fixed values of the hyperparameters. This section discusses how to obtain the hyperparameters Θ for a fixed training data set $D = \{\mathbf{x}_i, a_i\}_{i=1,\dots,n}$. Ideally integration over all possible hyperparameters should be done in order to obtain the best possible predictions of the function value a_{n+1} at damage level $n + 1$. Therefore, it can be written as,

$$f(a_{n+1}|D, \mathbf{x}_{n+1}, K(\cdot)) = \int f(a_{n+1}|D, \mathbf{x}_{n+1}, K(\cdot), \Theta) f(\Theta|D, K(\cdot)) d\Theta \quad (13)$$

The above integral is as complex as the integral given in Eq. (6) and also difficult to evaluate for a complex problem with several hyperparameters and a multiple input space. Out of the two possible approaches e.g., the Maximum evidence¹⁶ and the Monte Carlo¹⁷ approach only the use of the maximum evidence approach will be discussed to evaluate the integral. Using maximum evidence approach, Eq. (13) can be written in its approximate form as

$$f(a_{n+1}|D, \mathbf{x}_{n+1}, K(\cdot)) \cong f(a_{n+1}|D, \mathbf{x}_{n+1}, K(\cdot), \Theta_{MAP}) \quad (14)$$

The approximation in Eq. (14) is based on the assumption that the posterior distribution over Θ , i.e. $f(\Theta|D, K(\cdot))$, has a sharp peak around Θ_{MAP} . This approximation is generally reasonable¹³ and predictions are often found very close to those obtained using the true predictive distribution. Now to find the peak location of $f(\Theta|D, K(\cdot))$ the posterior of it needs to be optimized and the posterior distribution can be written as

$$f(\Theta|D, K(\cdot)) = \frac{f(\bar{\mathbf{a}}_n|\{\mathbf{x}_i\}_{i=1,2,\dots,n}, K(\cdot), \Theta) f(\Theta)}{f(\bar{\mathbf{a}}_n|\{\mathbf{x}_i\}_{i=1,2,\dots,n}, K(\cdot))} \quad (15)$$

In Eq.(15), the denominator (i.e., the evidence) is independent of Θ and can be ignored in the optimization process. On the other hand, the other two terms, the likelihood $f(\bar{\mathbf{a}}_n|\{\mathbf{x}_i\}_i, K(\cdot), \Theta)$, and the prior $f(\Theta)$, need to be considered in the optimization of $f(\Theta|D, K(\cdot))$. With the assumption that all $a_{i=1,2,\dots,n}$ damage indices follow a Gaussian distribution and using Eq.(8), the logarithm of the objective function can be written as

$$\begin{aligned} L \equiv \text{Log}(f(\Theta|D, K(\cdot))) = & - \frac{1}{2} \text{Log}(\det K_n) \\ & - \frac{1}{2} \bar{\mathbf{a}}_n^T K_n^{-1} \bar{\mathbf{a}}_n - \frac{n}{2} \text{Log}(2\pi) + \text{Log} f(\Theta) \end{aligned} \quad (16)$$

The log-likelihood function L in Eq.(16) is generally multi-modal and can be optimized using any multi-variate optimization algorithm. In the present work, the conjugate gradient method is used to optimize the log-likelihood function and to obtain the optimized hyperparameters. Note that it is common practice¹³ to ignore the log prior term in Eq.(16) due to the absence of knowledge on Θ . The resulting solution may not be always a realistic solution, however it can be assumed that $\text{Logf}(\Theta)$ is implicitly modeled through the optimization of the log-likelihood L .

5. Input-output data set for single step ahead prediction

For single step ahead prediction, the Gaussian process prediction model given by Eq.(8), only predicts single step ahead damage index. For prediction of the $n+1^{th}$ damage index, the training data set D and test input vector \mathbf{x}_{n+1} can be stated as,

$$D = \left[\mathbf{x}_i \mid a_i \right]_{i=d, \dots, n} = \begin{bmatrix} \overbrace{a_0 \quad a_1 \quad a_2 \quad \dots \quad a_{d-1}}^{\text{Training data matrix}} & \overbrace{a_d}^{\text{Target vector}} \\ a_1 & a_2 & a_3 & \dots & a_d & a_{d+1} \\ \vdots & \vdots & \vdots & \dots & \vdots & \vdots \\ a_{n-d} & a_{n-d+1} & a_{n-d+2} & \dots & a_{n-1} & a_n \end{bmatrix} \quad (17)$$

$$\mathbf{x}_{n+1} = \begin{bmatrix} \overbrace{a_{n-d+1} \quad a_{n-d+2} \quad a_{n-d+3} \quad \dots \quad a_n}^{\text{Test input data vector}} \end{bmatrix} \quad (18)$$

where in Eq. (17 and 18) the subscript n symbolizes the n^{th} damage instance or damage level, up to which the last on-line data was available, and d symbolizes dimension of the input space.

6. Input-output data set for multi step ahead prediction

For multi step ahead prediction, the GP model given by Eq.(8) recursively predicts the future state multi step ahead of the last on-line data available. However, unlike the single step ahead prediction case, the multi step ahead training data set D and test input vector $\mathbf{x}_{n+\bar{n}}$ are adaptively updated with off-line predicted damage indices rather than on-line estimated damage indices. For prediction of the $n + \bar{n}^{th}$ damage index $a_{n+\bar{n}}$ the training data set D and test input vector $\mathbf{x}_{n+\bar{n}}$ can be written as

$$D = \left[\mathbf{x}_i \mid a_i \right]_{i=d, \dots, n-1+\bar{n}} = \begin{bmatrix} \overbrace{a_0 \quad a_1 \quad a_2 \quad \dots \quad a_{d-1}}^{\text{Training data matrix}} & \overbrace{a_d}^{\text{Target vector}} \\ a_1 & a_2 & a_3 & \dots & a_d & a_{d+1} \\ \vdots & \vdots & \vdots & \dots & \vdots & \vdots \\ a_{n-d} & a_{n-d+1} & a_{n-d+2} & \dots & a_{n-1} & a_n \\ a_{n-d+1} & a_{n-d+2} & a_{n-d+3} & \dots & a_n & a_{n+1}^p \\ a_{n-d+2} & a_{n-d+3} & a_{n-d+4} & \dots & a_{n+1}^p & a_{n+2}^p \\ \vdots & \vdots & \vdots & \dots & \vdots & \vdots \\ a_{n-d-1+\bar{n}}^p & a_{n-d+\bar{n}}^p & a_{n-d+\bar{n}+1}^p & \dots & a_{n-2+\bar{n}}^p & a_{n-1+\bar{n}}^p \end{bmatrix} \quad (19)$$

$$\mathbf{x}_{n+\bar{n}} = \begin{bmatrix} \overbrace{a_{n-d+\bar{n}}^p \quad a_{n-d+\bar{n}+1}^p \quad a_{n-d+\bar{n}+2}^p \quad \dots \quad a_{n-1+\bar{n}}^p}^{\text{Test input data vector}} \end{bmatrix} \quad (20)$$

where in Eq. (19 and 20) the subscript n symbolizes the damage instance up to which the last on-line data is available, and the subscript \tilde{n} symbolizes the damage instance number following the availability of the last on-line data available, and the superscript p symbolizes predicted damage index from the off-line module, as opposed to being estimated from the on-line model.

7. Residual useful life estimation (RULE)

The residual useful life estimation can be defined as the difference between the number of fatigue cycles at which the predicted damage index becomes critical, i.e reaches its critical value (a^*), and the number of fatigue cycles at which the last on-line data is available. The RULE can be defined as:

$$RULE = (n + \tilde{n}^*)\Delta N - (n)\Delta N - N_0 = \tilde{n}\Delta N - N_0 \quad (21)$$

where ΔN is the number of fatigue cycle increments per each increment of damage instance and \tilde{n}^* corresponds to the number of damage instances for the damage index to become critical after the last available on-line data.

III. Numerical Results

A. Fatigue experiment and data collection

To numerically validate the integrated prognosis algorithm, a fatigue test was performed on a Al-6061 cruciform specimen under biaxial loading. The loaded cruciform specimen in a MTS biaxial fatigue test frame can be seen in Fig.3. The specimen was subjected to a constant amplitude fatigue loading with maximum amplitude (σ_{max}) 4 kips and load ratio $R=0.1$, and the biaxial machine actuator was operated with a frequency of 10 Hz. It is noted that, the maximum stress amplitude $\sigma_{max} = 4kips$ is equal to two third of the yield stress σ_Y . Based on nonlinear finite element analysis of cruciform specimen, the yield stress is approximated as $\sigma_Y = 6kips$. Also note that both the x-axis actuator and y-axis actuator of the biaxial frame was subjected to in-phase fatigue loading. For on-line state estimation, passive strain gauge sensors were used. One strain gauge is mounted on the horizontal flange (Fig. 4a), and one on the vertical flange (Fig. 4a) and two strain gauges are mounted on the web area (Fig. 4b) of the cruciform specimen. In addition, to the strain gauge sensors, piezoelectric (PZT-5H) sensors were also instrumented to collect the active sensing data. However, the active sensing data will be used in a future study. The current paper is based on strain gauge measurements. A hole in the center of the specimen was made to create crack initiation in the web area of cruciform specimen. To accelerate damage growth an EDM notch of 1 mm length was made at left quadrant boundary of the central hole (45° to the vertical axis). A 48 channel NI PXI system was used to collect the strain gauge signals, the piezoelectric sensor signals and the measurements from the biaxial machine load cells. In addition, a high resolution SONY camera was also used to visually monitor the crack growth. The data acquisition system and the computer capturing the visual image were synchronized with the biaxial machine controller to collect the time synchronized data/ image at a specified interval of $\Delta N = 1500cycles$. The data and image collection started at approximately 11 k cycles. The image and sensor data was collected at 47 different time instance. For the first 44 instances, the signals and images were collected while the biaxial machine was running and during the last three instances the data was collected when the machine was not running. This lead to a total of 44 different damage cases with the last damage state occurring at 75.5 kcycles. The developed real-time MATLAB based prognosis algorithm was also synchronized with the data acquisition system to estimate the current damage state, and to predict the future damage state and remaining useful life.

B. Correlation features and damage index

To evaluate the damage index as mentioned earlier, strain signal are mapped as input and output. For example, the signal (ϵ_x^F) from the strain gauge mounted on the horizontal flange (or X-arm) of the cruciform specimen is considered as the input signal u , whereas the signal (ϵ_x^W) from the web mounted stain gauge is considered as output v . It is noted that both the horizontal axis strain (ϵ_x^W) and the vertical axis strain (ϵ_y^W) are measured by two different strain gauges placed perpendicular to each other. Comparison of input strain (ϵ_x^F) and output strain (ϵ_x^W) is shown in Fig. 5. It presents a comparison for four different damage cases, damage case 7 (at 20 kcycle), damage case 20 (at 39.5 kcycle), damage case 42 (at 72.5 kcycle) and damage

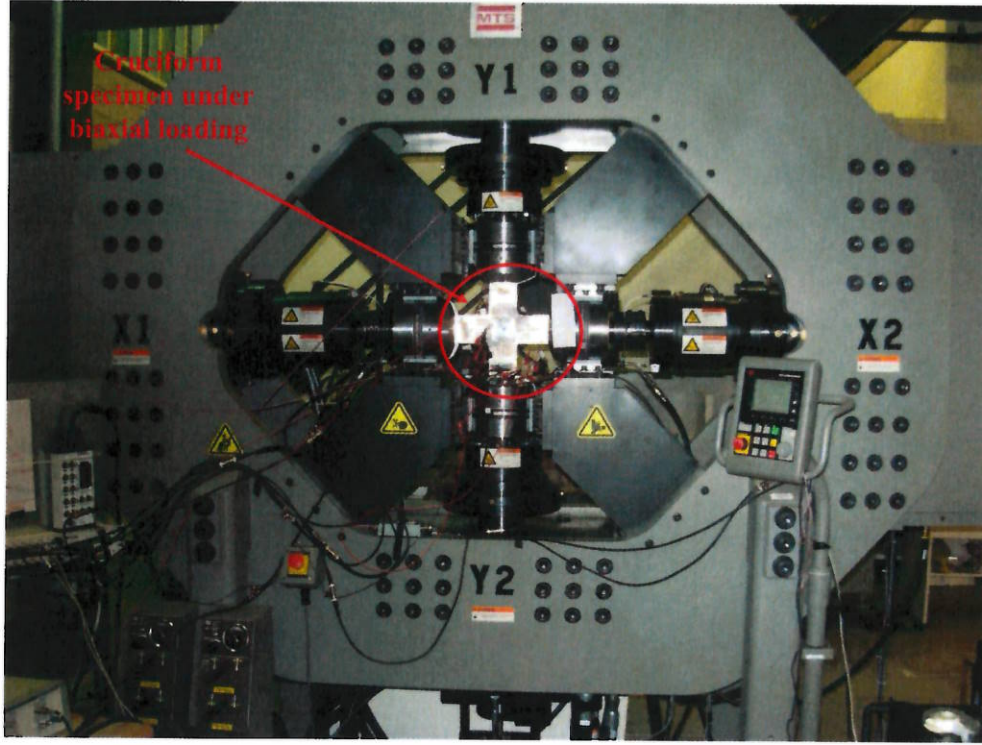


Figure 3. Al-6061 cruciform specimen loaded in a MTS biaxial fatigue test frame

case 44 (at 75.5 kcycle). From the figure it can be seen that though there is a clear trend between input and output strain during the later stages, the trend is hardly discernable in the earlier stages of damage growth. Rather than directly using the time series data for different damage case comparisons, using Eq. (4), the cross-correlation coefficient between input and output is found for different damage cases. The comparison of cross-correlation coefficients for damage level 1 (reference case at 11 k cycles) with cross-correlation coefficient at different damage levels are shown in Fig. 6. Figure 6a, 6b, 6c, and 6d, respectively show the comparison of cross-correlation coefficients of damage case 1 with damage case 7, damage case 20, damage case-42 and damage case-44. It is noted, the results shown in Fig.6, the x-axis flange strain (ϵ_x^F) and x-axis web strain (ϵ_x^W) are respectively taken as input u and output v . Also, it can be seen there is a better trend of damage condition, compared to the direct time series data from the strain gauges. However, to compare the different damage levels using a scalar quantity and to improve the discernability between different damage cases, the damage index proposed in Eq. (5), is evaluated for the different damage states. Figure 7 shows increase in the damage index with fatigue cycle for two different output measurements, ϵ_x^W and ϵ_y^W , for fixed input from x-axis flange measurement ϵ_x^F . The figure shows a clear trend of damage growth with ϵ_x^W as output strain. A good correlation between estimated damage index and normalized visual measurement is also observed. It must be noted that, the visual measurement is available up to damage level 29 (up to 53 kcycle). After the 29th damage level, it was found that the camera went out of focus. Figure 7 also shows that with respect to ϵ_y^W as the output strain, except for final failure regime, there is no clear trend in damage growth. This is because the input signal ϵ_x^F is poorly correlated with the y-axis web strain (ϵ_y^W) measurements. The higher damage indices during the final failure regime is possibly due to presence of shear strain components. In addition to the strain signal as input, a damage index is also obtained using biaxial frame load cell measurements (x-axis load cell). The new damage index is shown in Fig. 8, and a

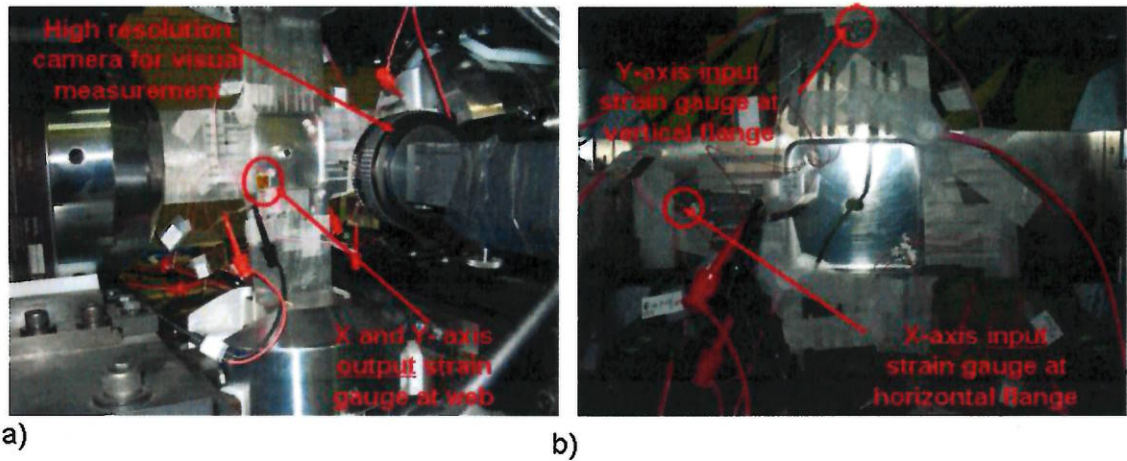


Figure 4. Undamaged and damaged condition of cruciform specimen: Plot-a shows the undamaged cruciform specimen. This rear view of the specimen also shows the location of two strain gauges mounted in the web area. Plot-b shows the final damage condition (at 75.5 kcycles) of the cruciform specimen. This front view of the specimen also shows the location of two strain gauges: one mounted on horizontal arm and the other mounted on the vertical arm of the specimen.

similar trend in damage index growth, as in the case of x-axis flange strain measurement as input, can be observed. However, it is noted that in a real life system, it is hardly possible to directly measure the loads applied to the structure. On the other hand, it is feasible to mount strain gauges or small sensors at required locations without affecting the structural integrity of the host structure. Therefore the results presented in the subsequent sections are based only on the strain gauge based data.

C. Single step ahead state prediction

Figure 9 shows the comparison between single step ahead prediction and actual damage index with on-line data available up to the previous damage level. As seen in the figure, the prognosis algorithm starts predicting from damage level 7. It is noted that the dimension d of the Gaussian process input is chosen as 6. Therefore the prognosis algorithm requires at least six damage states to obtain the 1×6 test input vector (see Eq. 18). Also, with unavailability of any training data set D (Eq. 17), to predict the 7^{th} damage state, the initial hyperparameters (Eq. 16) are chosen as: $\theta_n^p = \theta_n^w = 1$ and $\theta_n^g = 0.1$. Because of this, there is a large mismatch between the 7^{th} level damage prediction and the actual damage index. However, for prediction of damage level eight and beyond, the training input data matrix (Eq. 17) and target vectors (Eq. 18) are recursively updated. For each recursive updating, a new set of hyperparameters are obtained using the conjugate gradient method. Once the hyperparameters are estimated, the one-step ahead damage index is predicted for the following damage level. Figure 9 shows a clear correlation between one-step ahead predicted damage level and the actual damage index before the damage index reaches its critical value of 0.7. It must be noted that the actual damage indices are the on-line damage states (or damage index); these are directly estimated from the sensor signals. The threshold value of 0.7 is 70% of the final damage index value of 1. From Eq. (5) the damage index reaches its final value of 1 when there is no cross-correlation between the input u and v . This is because the specimen undergone complete failure. It is noted that choosing the critical damage index value of 0.7 is based on the results from previously performed similar experiments.

D. Multi step ahead prediction

Unlike the single step ahead prediction, the multi step ahead prediction recursively predicts the damage state ahead of the last online data availability stage. Figure 10 shows the multi step ahead state prediction. Similar to single step ahead prediction process, the prognosis algorithm initiates after the 6^{th} damage level (at 18.5 kcycles). From the 7^{th} damage level (from 20kcycles), damage indices are predicted and then fed back to the prognosis model to update the training data matrix (Eq. 19) and the test input vector (Eq. 20).

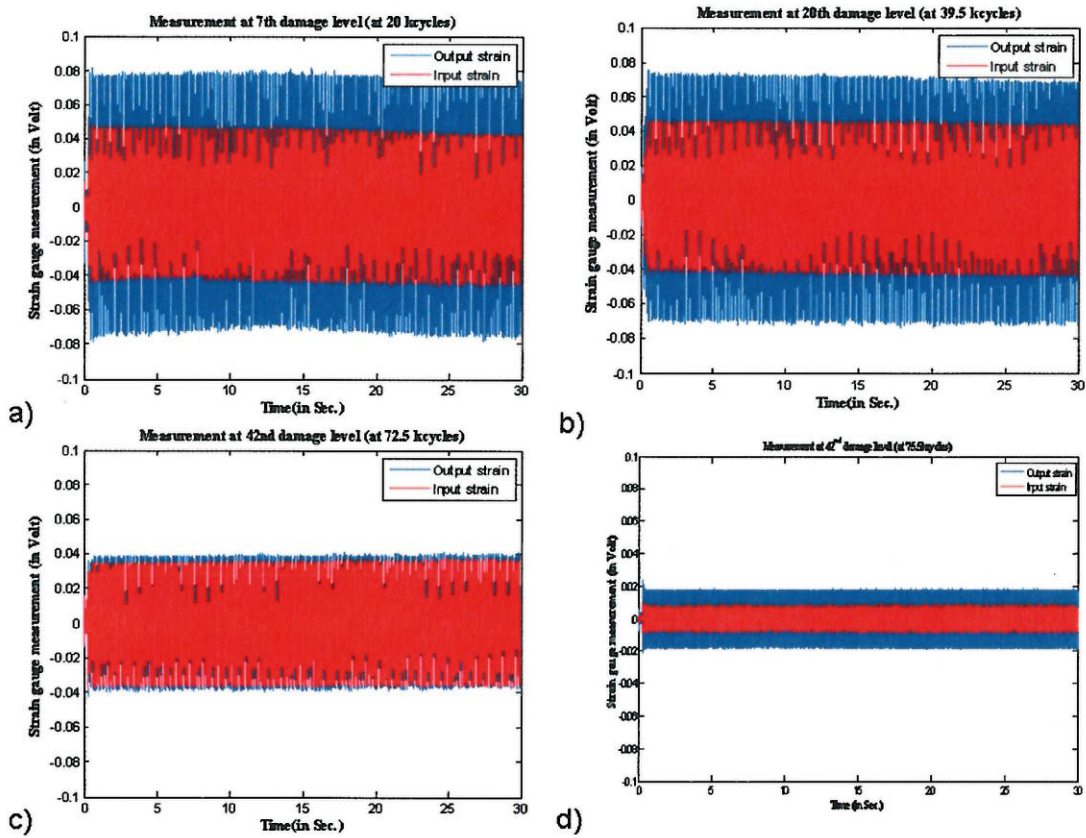


Figure 5. Input output strain comparisons at different damage levels.

The feedback process is continued recursively as long as the predicted damage index does not reach its critical value of 70% of its final failure value. It is to be noted that unlike single step ahead prediction, the training data matrix and the test input vector are updated with off-line model predicted states, rather than being updated with on-line model estimated states. It can be seen from Fig. 10 that up to damage level 23 (at 44 kcycles) the multi step ahead prediction fails to reach the critical damage index. This is because the predictive model, which is unable to learn the damage growth dynamics. To reduce the computational expenses, the prognosis algorithm was stopped at certain times. The criteria for stopping the algorithm was if the rate of damage index growth is not greater than $1 \times 10^{-7}/cycles$ for six consecutive damage levels, the off-line predictive model is terminated. This is because, physically, if the damage growth is so slow the damage index value, will never reach the critical value even if the algorithm were to run indefinitely. From Figure 10 it is also seen that, the first multi step ahead prediction curve, that reaches the critical value starts from damage level 24 (from 45.5 kcycles). Beyond this damage level, the multiple step ahead prediction increasingly converges with the actual damage index. Also, it can be assumed that the prediction horizon is between damage level 24 (45.5 kcycles) and damage level 42 (72.5 kcycles), at which the on-line model estimation states reaches its critical value.

E. Residual useful life estimation (RULE) and mean square error evaluation

Using Eq. (21), the residual useful life at a given damage level (up to which the last online data was available) is estimated. Figure 11 shows the comparison of predicted RULE and actual RULE. From the figure it can be seen that, there is a good correlation between predicted and actual RULE in the true positive regime i.e., between damage level 24 (at 45.5 kcycles) and damage level 42 (at 72.5 kcycles). Also it can be observed

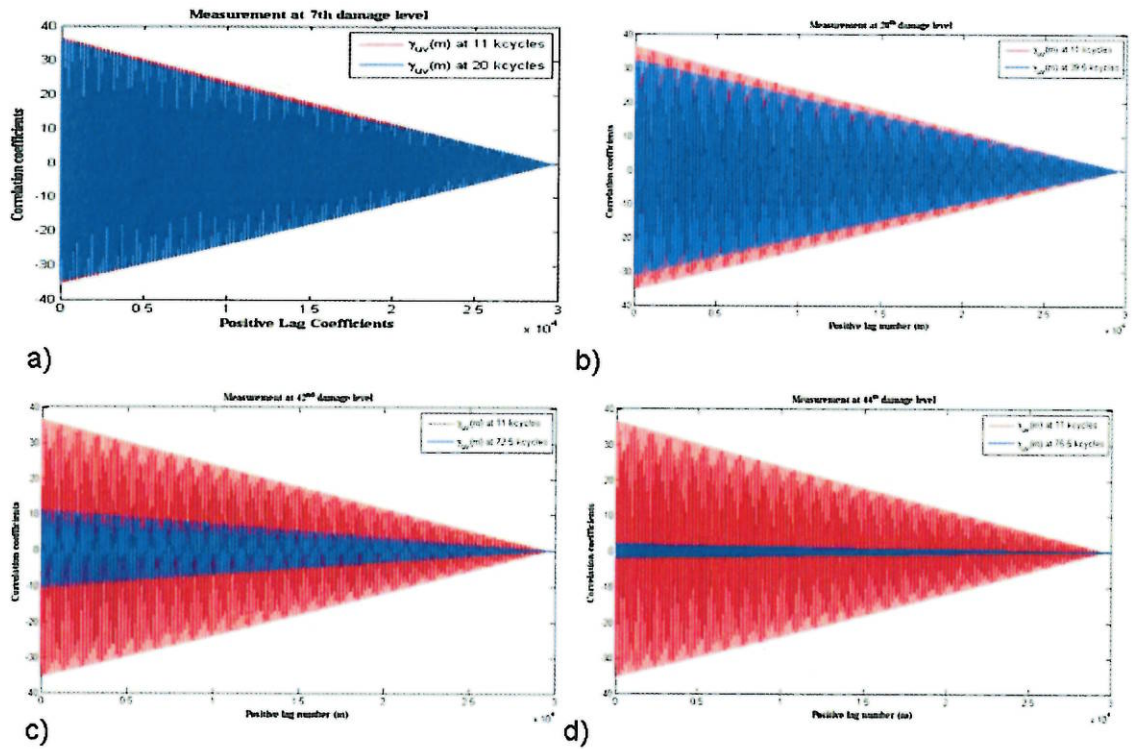


Figure 6. Cross-correlation coefficient comparison at different damage levels with the reference level at 11 cycles

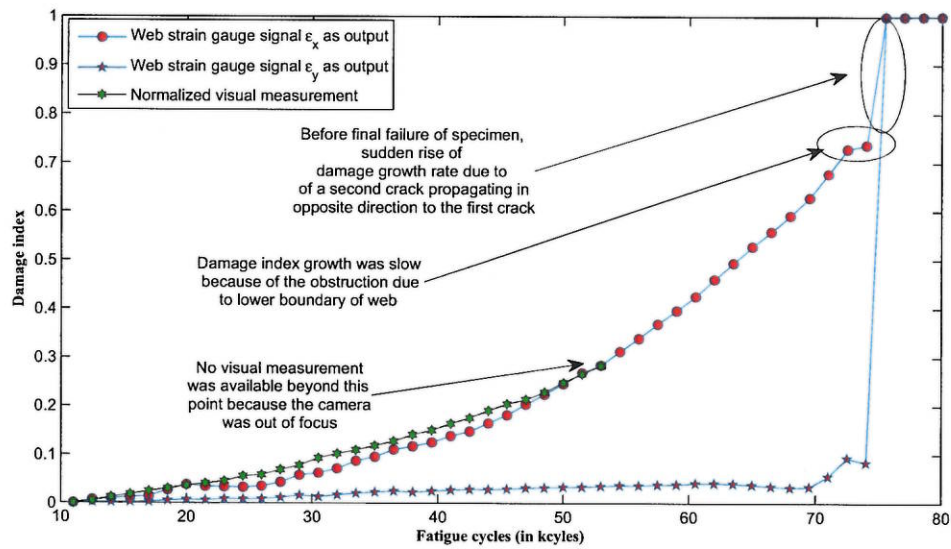


Figure 7. Variation of damage index with fatigue cycle. Flange (x-axis) strain measurements are used as input and web (x-axis) strain measurements as output

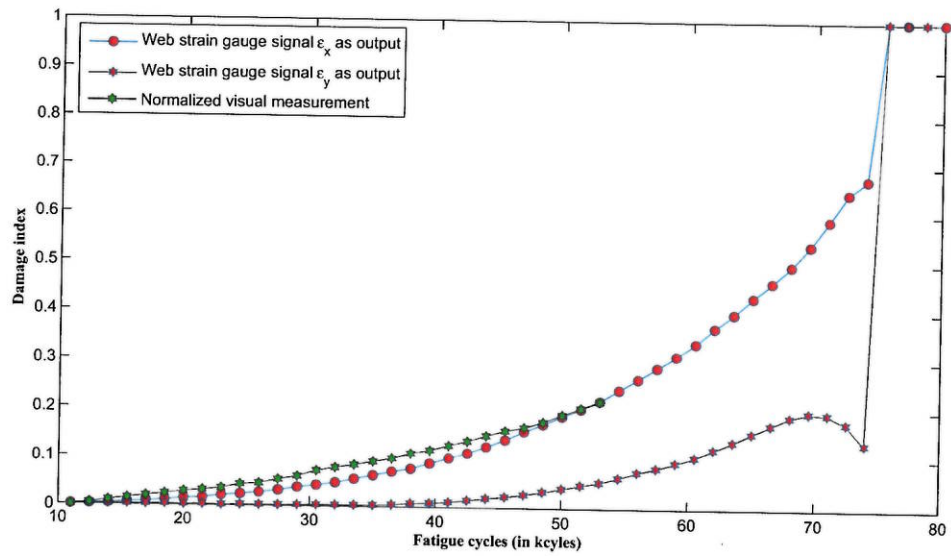


Figure 8. Damage index with x-axis biaxial frame load-cell measurements as input and web (x-axis) strain measurements as output

that as more and more online data becomes available, better correlation between predicted RULE and actual RULE is obtained. Figure 12 shows the mean square error between predicted RULE and estimated RULE. It can be seen that during the true positive regime, the mean square error is substantially reduced compared to the mean square error during the false positive regime.

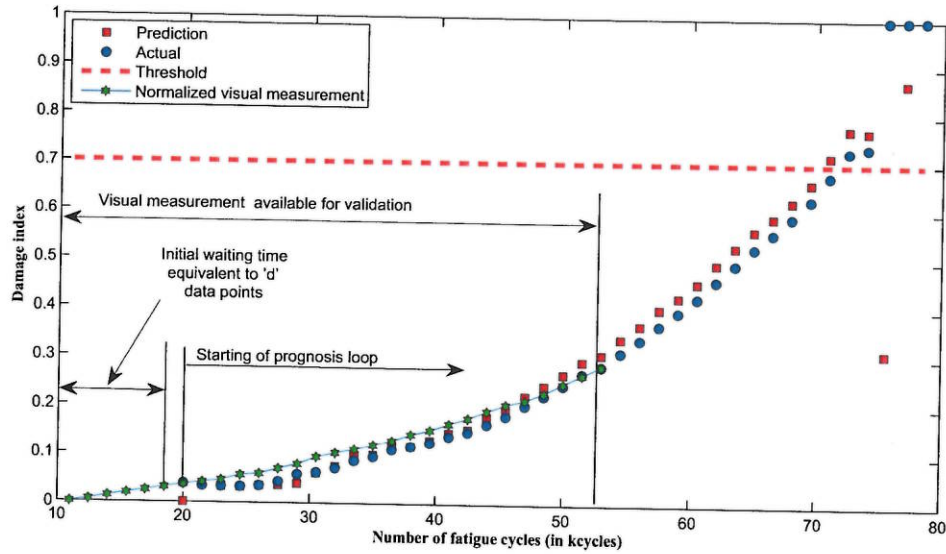


Figure 9. Off-line model prediction of one-step ahead damage state.

IV. Conclusion

An adaptive on-line off-line life integrated predictive model has been developed for applications to Structural Health Monitoring and damage prognosis. The developed prognosis model combines an on-line state estimation model with an off-line predictive model to adaptively estimate the residual useful life of an Al-6061 cruciform specimen under biaxial loading. Some important features of this algorithm and observation from this study are summarized below.

1. The on-line model is based on a non-parametric system identification approach, which estimates the current damage states. The numerical results showed good correlation between on-line estimated state and the normalized visual measurements.
2. Once the current damage state was available from the on-line model, the information was fed to an off-line predictive model to obtain the future states and remaining useful life estimation (RULE).
3. The off-line predictive model is a high-dimensional kernel function based recursive Gaussian process model.
4. The future states are recursively predicted by feeding back the previous predicted states to the off-line model. Also, the model parameters (Gaussian process hyperparameters) are updated with repetitive conjugate gradient based optimization.
5. Good correlation was observed between actual damage states and predicted future damage states between the 24th damage level (at 45.5 kcycles) and the 41st (at 71 kcycles) damage level at which the damage index reaches its critical value of 0.7.
6. The duration between the 24th damage level (at 45.5 kcycles) and the 42nd damage level (at 72.5 kcycles) was considered as true positive regime or prediction horizon. This regime also showed that a good correlation between predicted RULE and actual RULE.

Acknowledgments

This research was supported by the MURI and the DURIP Program, Air Force Office of Scientific Research, grant number: FA9550-06-1-0309 and FA9550-07-1-0508; Technical Monitor, Dr. Victor Giurgiutiu.

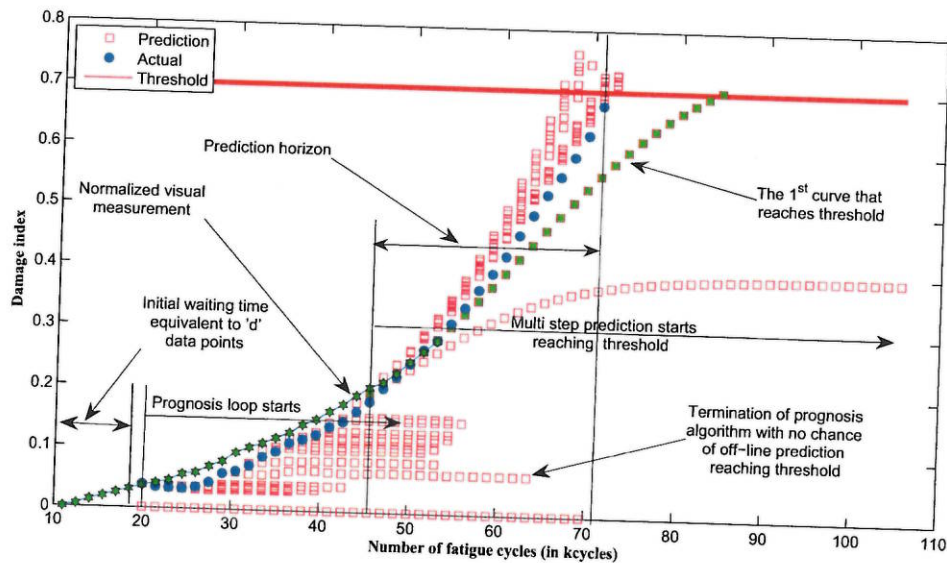


Figure 10. Off-line model prediction of multi step ahead damage state.

References

- ¹Iyyer, N., Sarkar, S., Merrill, R., and Phan, N., *Aircraft life management using crack initiation and crack growth models - P-3C Aircraft experience*, International Journal of Fatigue 29 (2007) 1584-1607.
- ²Newman, J.C. Jr. 1992. FASTRAN-II - A Fatigue Crack Growth Structural Analysis Program. NASA Technical Memorandum 104159, Langley Research Center.
- ³Harter, J.A. 1999, AFGROW Users' Guide and Technical Manual. Report No. AFRL-VA-WP-1999-3016, Air force Research Laboratory.
- ⁴Wu, W. F., and Ni, C.C., *Probabilistic models of fatigue crack propagation and their experimental verification*, Probabilistic Engineering Mechanics 19 (2004) 247-257.
- ⁵Liu, Y., and Mahadevan, S., *Stochastic fatigue damage modeling under variable amplitude loading*, International Journal of Fatigue 29 (2007) 1149-1161.
- ⁶Gupta, S., and Ray, A., *Real-time fatigue life estimation in mechanical structures*, Meas. Sci. Technol. 18 (2007) 1947-1957.
- ⁷Mohanty, S., Chattopadhyay, A., Peralta, P., Das, S., and Willhauck, C., *Fatigue Life Prediction Using Multivariate Gaussian Process*, AIAA/ASME/ASCE/AHS/ASC Structures, Structural Dynamics, and Materials Conference, Schaumburg, Illinois, April, 7-10, 2008.
- ⁸Mohanty, S., Chattopadhyay, A., and Peralta, P., *On-line Life Prediction of a Structural Hot-Spot*, ASME Conference on Smart Materials, Adaptive Structures and Intelligent Systems, October 28-30, 2008, Ellicott City, MD.
- ⁹Farrar, C.R., Sohn, H., Hemez, F.M., Anderson, M.C., Bement, M.T., Cornwell, P.J., Doebling, S. W., Schultze, J.F., Lieven, N., and Robertson, A.N., 2003, *Damage Prognosis: Current Status and Future Needs*, Los Alamos Report No. LA-14051-MS.
- ¹⁰Farrar, C.R., Worden, K., Todd, M.D., Park, G., Nichols, J., Adams, D.E., Bement, M.T., Farinholt, K., 2007, *Nonlinear System Identification for Damage Detection*, Los Alamos Report No. LA-14353.
- ¹¹Mohanty, S., Das, S., Chattopadhyay, A., and Peralta, P., "Gaussian Process Time Series Model for Life Prognosis of Metallic Structure", 2009, Accepted for publication in *Journal of Intelligent Material Systems and Structures*.
- ¹²Billington, S., Zhang, C., Kurfess, T., Danyluk, S., Liang, S., *Adaptive prognostics for rolling element bearing conditions*, Mechanical Systems and Signal Processing, 1999, 13(1), 103-113.
- ¹³Gibbs, M.N. 1997. "Bayesian Gaussian Processes for Regression and Classification," PhD thesis, Department of Physics, University of Cambridge.
- ¹⁴MacKay, D.J.C. 1998. "Introduction to Gaussian Processes," In C. M. Bishop, editor, *Neural Networks and Machine Learning*, 168:133-165. Springer, Berlin.
- ¹⁵Rasmussen, C. and Williams, C. 2006. , Gaussian Processes for Machine Learning, The MIT Press, Cambridge, MA.
- ¹⁶MacKay, D.J.C., *Bayesian Interpolation*, Neural Computation, 4(3): 415-447, 1992.
- ¹⁷Neal, R. M. 1993. *Probabilistic Inference Using Markov Chain Monte Carlo Method*, Technical Report CRG-TR-93-1, Dept. of Computer Science, University of Toronto.
- ¹⁸Christopher K. I. Williams. *Computing with infinite networks* Edited by Michael C. Mozer, Michael I. Jordan, and Thomas Petsche, *Advances in Neural Information Processing Systems*, MIT Press, Cambridge, MA, 1997, Vol. 9.

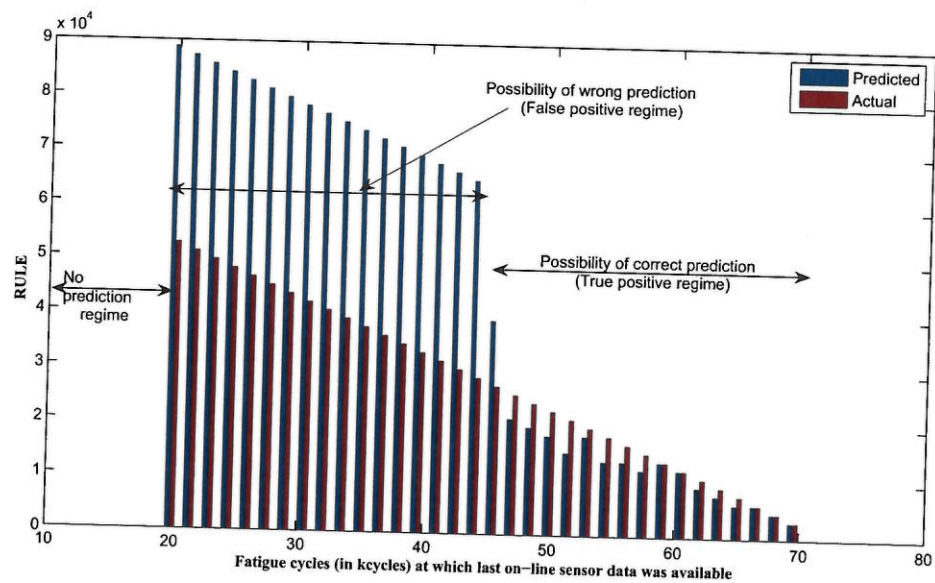


Figure 11. Comparison of predicted RULE and actual RULE.

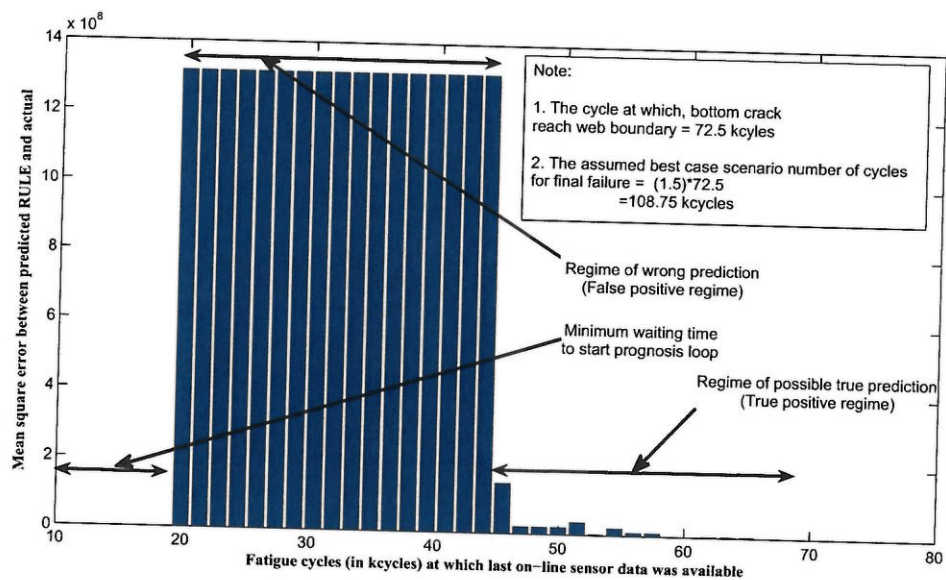


Figure 12. Mean square error between predicted RULE and actual RULE.